Engineering Journal

Fourth Quarter 2020 | Volume 57, No. 4

AISC

Smarter.
Stronger.
Steel.

Technical Note

Steel Structures Research Update

Errata

Engineering Journal

American Institute of Steel Construction

Dedicated to the development and improvement of steel construction, through the interchange of ideas, experiences and data.

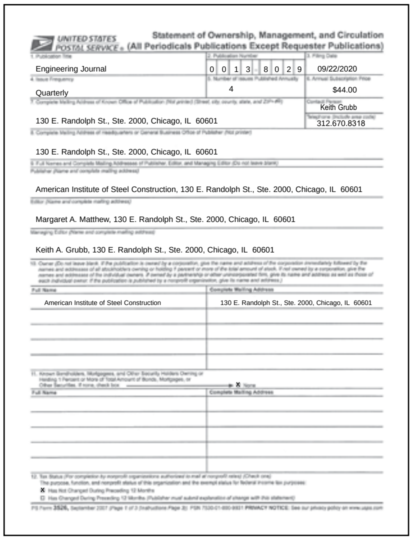

UNITED STATES POSTAL SERVICE®

Statement of Ownership, Management, and Circulation (All Periodicals Publications Except Requester Publications)

1. Publication Title Engineering Journal	2. Publication Number 0 0 1 3 - 8 0 2 9	3. Filing Date 09/22/2020
4. Issue Frequency Quarterly	5. Number of Issues Published Annually 4	6. Annual Subscription Price $44.00

7. 130 E. Randolph St., Ste. 2000, Chicago, IL 60601

Contact Person: Keith Grubb

Telephone (Include area code): 312.670.8318

8. 130 E. Randolph St., Ste. 2000, Chicago, IL 60601

9. Publisher: American Institute of Steel Construction, 130 E. Randolph St., Ste. 2000, Chicago, IL 60601

Editor: Margaret A. Matthew, 130 E. Randolph St., Ste. 2000, Chicago, IL 60601

Managing Editor: Keith A. Grubb, 130 E. Randolph St., Ste. 2000, Chicago, IL 60601

10. Owner

Full Name	Complete Mailing Address
American Institute of Steel Construction	130 E. Randolph St., Ste. 2000, Chicago, IL 60601

11. Known Bondholders, Mortgagees, and Other Security Holders Owning or Holding 1 Percent or More of Total Amount of Bonds, Mortgages, or Other Securities. If none, check box → ☒ None

12. Tax Status

☒ Has Not Changed During Preceding 12 Months

☐ Has Changed During Preceding 12 Months

PS Form 3526, September 2007 (Page 1 of 3)

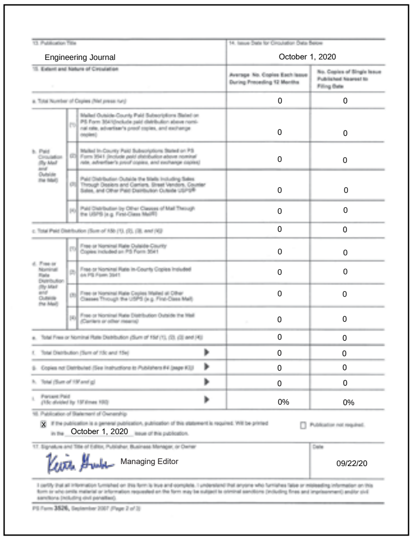

13. Publication Title Engineering Journal	14. Issue Date for Circulation Data Below October 1, 2020	
15. Extent and Nature of Circulation	Average No. Copies Each Issue During Preceding 12 Months	No. Copies of Single Issue Published Nearest to Filing Date
a. Total Number of Copies (Net press run)	0	0
b. Paid Circulation (1)	0	0
b. Paid Circulation (2)	0	0
b. Paid Circulation (3)	0	0
b. Paid Circulation (4)	0	0
c. Total Paid Distribution	0	0
d. Free or Nominal Rate Distribution (1)	0	0
d. Free or Nominal Rate Distribution (2)	0	0
d. Free or Nominal Rate Distribution (3)	0	0
d. Free or Nominal Rate Distribution (4)	0	0
e. Total Free or Nominal Rate Distribution	0	0
f. Total Distribution	0	0
g. Copies not Distributed	0	0
h. Total	0	0
i. Percent Paid	0%	0%

16. Publication of Statement of Ownership

☒ in the October 1, 2020 issue of this publication. ☐ Publication not required.

17. Managing Editor — Date: 09/22/20

PS Form 3526, September 2007 (Page 2 of 3)

Manuscripts are welcomed, but publication cannot be guaranteed. All manuscripts should be submitted in duplicate. Authors do not receive a remuneration. Guidelines for authors are printed on the inside back cover.

Engineering Journal (ISSN 0013-8029) is published quarterly. Subscriptions: Members: one subscription, $40 per year, included in dues; Additional Member Subscriptions: $40 per year. Non-Members U.S.: $160 per year. Foreign (Canada and Mexico): Members $80 per year. Non-Members $160 per year. Published by the American Institute of Steel Construction at 130 E Randolph Street, Suite 2000, Chicago, IL 60601.

Periodicals postage paid at Chicago, IL and additional mailing offices. **Postmaster:** Send address changes to *Engineering Journal* in care of the American Institute of Steel Construction, 130 E Randolph Street, Suite 2000, Chicago, IL 60601.

Subscriptions: subscriptions@aisc.org, 312.670.2400

Archives: Search at **aisc.org/ej**. Article downloads are free for current members and are avaialable for a nominal fee for non-members.

Experimental Investigation of a Self-Centering Beam Moment Frame

MATTHEW R. EATHERTON and ABHILASHA MAURYA

ABSTRACT

The self-centering beam (SCB) is a shop-fabricated unit that can be implemented in moment-resisting frames using conventional field construction methods to minimize permanent residual drifts after earthquakes and concentrate seismic damage in replaceable elements. An experimental program was conducted on five SCB specimens that were approximately two-thirds scale relative to a prototype building. The results showed that the beam end moments are not equal, as much as 60% different at peak moment, so total flexural strength, calculated as the sum of the moments at both ends, is a better way to characterize SCB flexural strength. Using this approach, the proposed equation to predict flexural strength exhibited an average error of 5% compared to the tests. The SCB was shown to have exceptional deformation capacity as the specimens were subjected to as much as 6% story drift, and the detailing was shown effective at concentrating inelasticity in the replaceable energy dissipating elements. The proposed design procedure is shown capable of controlling the story drift associated with undesirable limit states, limiting story drifts at zero force (eliminate residual drifts), and producing no observable inelasticity outside the energy-dissipating element at design level drifts.

Keywords: self-centering, seismic behavior, large-scale experiments, buckling restrained brace, moment frame, structural fuses.

INTRODUCTION

Conventional seismic force-resisting systems use inelasticity in structural members and connections to create ductility, dissipate seismic energy, and provide protection against collapse. For example, steel moment-resisting frames (MRFs) are designed to develop plastic hinges near the beam ends to facilitate inelastic deformation capacity. A consequence of this design methodology is that conventional seismic systems do not explicitly limit the amount of structural damage or offer a repair method that allows continued use of a structure after an earthquake. Yielding, buckling, or fracture of structural elements also leads to permanent horizontal displacements, referred to as residual story drift. Repairing earthquake-related structural damage is expensive and time-consuming because the damage is often distributed throughout the structure in many nonreplaceable elements, and if the damage or residual drifts are significant enough, it becomes more economical to demolish the building and rebuild.

To achieve earthquake performance goals related to reducing business downtime and repair costs (or, looking at it in another way, improving structural repairability and probability for continued building use), it is necessary to eliminate residual drifts and concentrate structural damage in elements that either do not experience significant cyclic degradation or are replaceable. Over the past three decades, a number of self-centering seismic systems have been developed to fill this need. Self-centering seismic systems can be broadly grouped into three categories: rocking structural systems (Eatherton et al., 2014), self-centering braces (Miller et al., 2012), and self-centering moment frames (Ricles et al., 2001). Although the configurations vary, the majority of these systems consist of the same two fundamental components: (1) an elastic restoring force mechanism, whereby a post-tensioning or gravity force acts to close a gap that is allowed to form between two elements, and (2) an energy-dissipating mechanism associated with yielding or friction that uses replaceable elements if damage is expected.

As described in more detail in the next section, steel self-centering moment-resisting frames have been developed wherein steel beams are clamped to the side of steel columns with horizontal post-tensioning. During lateral loading, a gap forms between the end of the beam and the column, and the post-tensioning acts to close this gap when lateral loads are removed, thus creating a restoring force (Ricles et al., 2001). The gap opening at the beam-to-column connection, however, causes the center of the beam end to displace laterally relative to the face of the column. These gap openings have the cumulative effect of increasing the width of the moment frame, which hinders the self-centering capabilities of the system and causes damage to the floor system (MacRae and Gunasekaran, 2006). Although schemes for accommodating the expansion of the floor plate have

---

Matthew R. Eatherton, PhD, SE, Associate Professor, Department of Civil Engineering, Virginia Tech, Blacksburg, Va. Email: meather@vt.edu (corresponding)

Abhilasha Maurya, PhD, Design Engineer, Walter P. Moore, Houston, Texas. Email: abhilashamaurya@gmail.com

Paper No. 2019-12

been proposed (Garlock and Li, 2008), they often require the structural beams to be disconnected from the diaphragm over large parts of the floor.

Deformation incompatibility between the self-centering connections and the diaphragm are just one factor that is impeding the implementation of steel self-centering moment frames in practice. Other factors include complex field construction that requires field erection methods uncommon in steel buildings such as setting post-tensioning strands and anchorage, field fit-up of sensitive bearing surfaces, and post-tensioning procedures.

Darling et al. (2013) first proposed a self-centering beam that mitigates many of these challenges by bundling the restoring force mechanism and energy dissipation elements into a self-contained, shop-fabricated unit that can be erected using conventional means. In the present study, large-scale experiments are conducted on five specimens that are two-thirds scale relative to a prototype building. Design parameters such as initial post-tensioning stress, beam depth, and yield strength of the energy dissipating element are varied to evaluate their effect on self-centering beam behavior. The tests are also used to validate the performance of the self-centering beam as well as investigate the performance of the local details.

BACKGROUND ON SELF-CENTERING MOMENT FRAMES

Research on self-centering moment frames started in the 1990s with two research programs studying post-tensioned precast concrete structures. A large research program called the Precast Seismic Structural Systems (PRESSS) program was started in 1990 (Priestley, 1991), while research was also being conducted at NIST (Stone et al., 1995). A hybrid moment-resisting precast concrete beam-to-column connection was developed, which consists of a precast concrete beam post-tensioned to a precast column with mild steel reinforcing bars that yield and dissipate energy. Between the two projects, considerable research was conducted, including large-scale cyclic subassemblage testing (Stone et al., 1995), lateral load testing on full buildings (Priestley et al., 1999), and substantial computational studies (El-Sheikh, 1997). Related research was later conducted on coupled concrete shear walls with steel beams that were post-tensioned between reinforced concrete shear walls (Kurama et al., 2006). This research on post-tensioned precast moment frames led to proposed design procedures (Hawkins and Ghosh, 2004); design requirements (ACI, 2003); and, ultimately, to implementation in actual buildings, including a 39-story tall apartment tower in San Francisco (Englekirk, 2002) and a university building and hospital building in New Zealand (Buchanan et al., 2011).

Similarly, there has been substantial research on self-centering steel moment frames starting in the 2000s. Some of the first work was conducted at Lehigh University on steel beams post-tensioned to a steel column using post-tensioning strands and incorporating various energy dissipating mechanisms such as yielding angles (Ricles et al., 2001), bolted friction devices at the bottom flange (Wolski et al., 2006), and bolted friction devices in the web (Lin et al., 2013). At approximately the same time, a similar connection configuration was being studied by Christopoulos et al. (2002) that used post-tensioning bars and buckling restrained yielding bars, although later they investigated this configuration with friction devices at the flanges (Kim and Christopoulos, 2008). A substantial amount of research on self-centering steel frames has also been conducted in Taiwan, including subassemblage testing (Chou et al., 2006), tests with composite slabs (Chou et al., 2008), shake table testing (Chou and Chen, 2011a), and variations in the energy dissipation element (Chou and Lai, 2009). Beyond these three groups (Lehigh, Christopoulos, and Taiwan), there have been studies with variations on the energy dissipation element (web hourglass pins, Vasdravellis et al., 2013) and end-plate moment connections with shape memory alloy bolts (Fang et al., 2018; Farmani and Ghassemieh, 2016).

Although there has been considerable research on steel self-centering moment frames, they have not been included in code provisions, nor have they seen acceptance in practice. Perhaps one of the primary issues holding this system back from adoption is deformation incompatibility with gravity framing. As gaps open between the beams and columns, the frame expands horizontally, causing damage to the diaphragm; conversely, the diaphragm hinders the gap opening, thus disrupting the restoring force mechanism. Experiments with composite slabs verify that the slabs significantly alter the behavior of these steel self-centering moment connections (Chou et al., 2008). Complicated schemes have been proposed to detach the diaphragm from parts of the structural framing (Garlock et al., 2007; Kim and Christopoulos, 2009; Chou and Chen, 2011b) or design the connection for slab effects (Chou et al., 2008).

Alternatively, three solutions have been proposed as ways to implement post-tensioned steel moment frames without deformation incompatibility with the diaphragm. First, post-tensioned steel connections have been proposed and tested that pivot about the top flange (Dowden and Bruneau, 2011). Although this type of connection does not suffer from deformation incompatibility issues, it does not have a gap-opening mechanism nor a bilinear elastic response, thus requiring energy dissipation elements with very little resistance against restoring force to approximate a self-centering system. A second alternative is the self-centering modular panel consisting of a self-contained, one-bay, self-centering moment frame that fits between the structural beams of a building (Wang et al., 2017). Because the gap-opening mechanism is separated from the structural frame, it does not create any deformation incompatibility with the diaphragm. However, the self-centering modular panel does not allow an open bay like a typical moment frame and thus must be used in architecturally solid walls.

The third alternative is the self-centering beam, which is the focus of this paper. Besides the initial work (Darling et al., 2013; Maurya and Eatherton, 2016), other researchers have explored the distribution of moment between the two ends of the self-centering beam (Huang et al., 2017) and created new configurations of self-centering beams (Lin, 2015; Huang et al., 2019).

DESCRIPTION OF THE SELF-CENTERING BEAM

The self-centering beam (SCB) as shown in Figure 1 incorporates both the restoring force mechanism and the energy dissipating elements into one self-contained unit (i.e., the force-restoring mechanism and energy dissipation are built in) that can be prefabricated (i.e., manufactured in a shop and brought to the construction site). The body of the SCB is made of a wide-flange, I-shaped beam. Two concentric tubes are located at the bottom flange with the outer tube welded to the I-shaped beam, and the inner tube connected to the columns using pinned connections that are allowed to rotate in the plane of the SCB. Horizontal post-tensioning (PT) strands are anchored at each end at thick anchorage plates that are allowed to slide over the pieces connecting the inner tube to the columns. During construction, the PT strands are stressed to approximately 20% to 60% of their ultimate strength, and this stress acts to keep the inner and outer tubes in alignment.

When subjected to story drift, the columns apply a racking motion to the SCB, whereby the wide-flange beam and outer tube move in one direction (to the right in Figure 1), and the inner tube is forced to move relative to the outer tube (e.g., to the left in Figure 1), thus creating a telescoping (i.e., relative movement) of the tubes relative to one another. This telescoping motion causes a gap to form between one of the tubes and the anchorage plate at one end (between the outer tube and anchorage plate at the left end) and the other tube and anchorage plate at the other end (between the inner tube and anchorage plate at the right end). Regardless of the direction of story drift, the anchorage plates are forced apart and the PT strands elongate, creating additional force that acts to close the gaps. The configuration of concentric tubes with PT strands acting to keep them in alignment is the restoring force mechanism for the SCB.

Separately, replaceable energy dissipating elements are included in the form of miniature buckling restrained braces (MBRBs) (Maurya et al., 2016). The MBRBs are connected to the inner tube at one end and the outer tube at the other so that they experience axial deformation as the tubes undergo the telescoping motion. The MBRBs have been shown in prior research to be capable of large deformations of up to 4% average strain in the core plate and cumulative plastic deformations up to 400 times the yield deformation. In Figure 1, the energy dissipation elements are shown on the

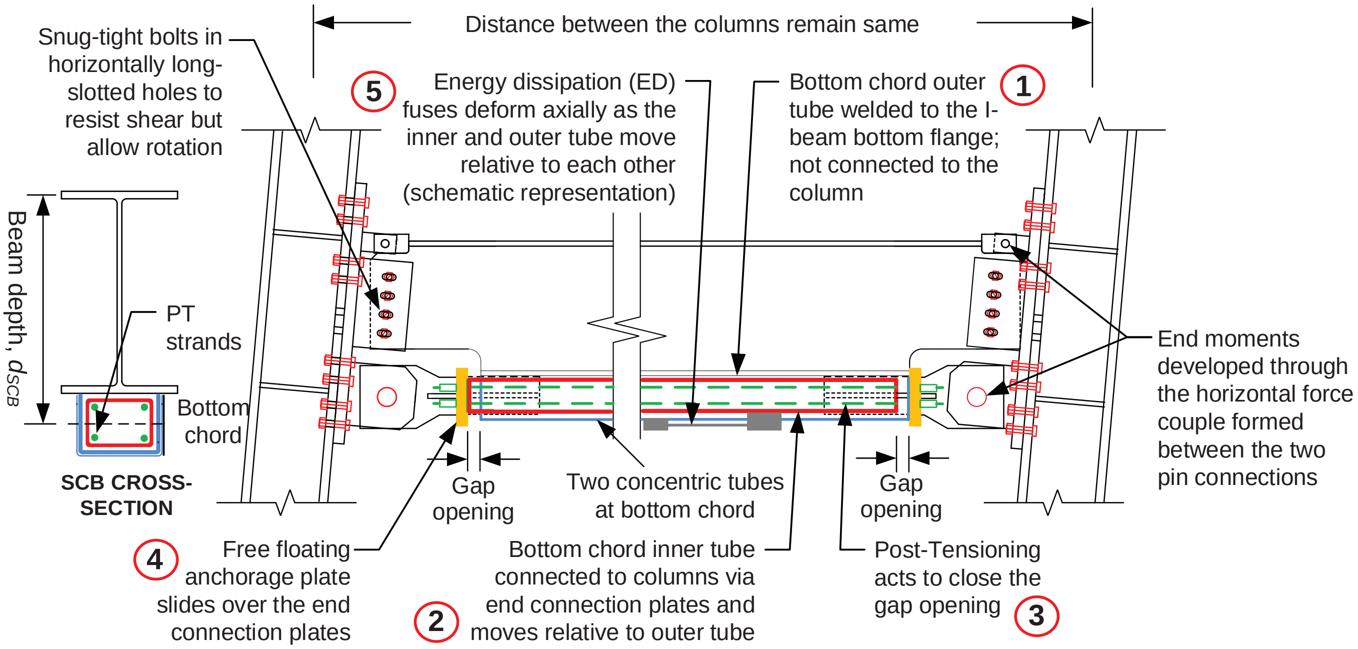

Fig. 1. Diagram of self-centering beam (SCB).

bottom of the SCB, but in construction, multiple MBRBs were implemented on the sides of the tubes as will be shown in a later section.

It is expected that this configuration of self-centering beam, as well as variations on the SCB (Darling et al., 2013; Lin, 2015; Huang et al., 2019), offer several key advantages as compared to some other self-centering seismic systems. First, the gap-opening mechanism is internal to the SCB in a way that allows the distance between columns to stay constant. This eliminates the deformation incompatibility issues that arise in other self-centering moment frames when the gap-opening mechanism causes forces and damage in the floor slab or surrounding gravity framing. Second, the SCB can be prefabricated in a shop where the fit-up of sensitive bearing surfaces and post-tensioning operations can be conducted in a controlled environment. Lastly, the SCB can be erected in the field using conventional construction methods such as bolting or welding. The configuration shown in Figure 1 uses a field-bolted end plate connection, but configurations with field-welded connections to the column are also viable.

GLOBAL BEHAVIOR AND SYSTEM EQUATIONS OF SCB

The idealized behavior of the SCB moment frame (along with the component behavior of the post-tensioned beam and MBRBs) when subjected to cyclic loading is shown in Figure 2. After the loading begins at point A, the stiffness is primarily controlled by the geometry of the SCB body (W-section and the concentric tubes) as the tubes decompress. Once the lateral force becomes large enough that the end moments overcome the pre-compression force provided by the PT strands, gap opening occurs between the anchorage plates and the tubes, marked as point B in Figure 2. The gap opening causes a softening of the system load-deformation response that is evident from the decrease in the stiffness of the SCB moment frame as shown in Figure 2(c). This reduction in stiffness is desirable because it limits the forces that can develop in the columns and foundation (i.e., softening occurs without structural damage). The telescopic movement of the tubes after the gap opening causes axial deformation of the MBRBs and eventually leads to their yielding, marked as point C in Figure 2. The stiffness of the system after MBRB yielding is controlled by the axial stiffness of the PT strands, post-yield stiffness of the MBRBs, and the effective depth of the SCB, d_{SCB}, shown in Figure 1. After load reversal (point D), the MBRBs yield in the opposite direction (point F) and the gap closes at point G. Finally, at the end of the loading cycle (point H), the SCB returns to its original position with near-zero drift.

To design the SCB and understand its behavior, it is necessary to develop parameters and associated equations to describe flexural strength, self-centering capability, and drift at which brittle limit states occur. A free-body diagram of the two parts of the SCB is shown in Figure 3 for the state after gap opening has occurred. In this figure, with drift to the right, the PT strands exert force, F_{PT}, on the inner tube at the left end and outer tube at the right end. With the configuration and loading shown in Figure 3, the MBRB is in tension and exerts a force, F_{fuse}, on the outer tube and inner tube. The top of the SCB is attached to the columns and experiences reaction forces, F_{TL} and F_{TR}, on the left and right ends, respectively, whereas the inner tube is connected to the columns at the bottom and experiences reaction forces, F_{IL} and F_{IR}, on the left and right ends, respectively. The vertical

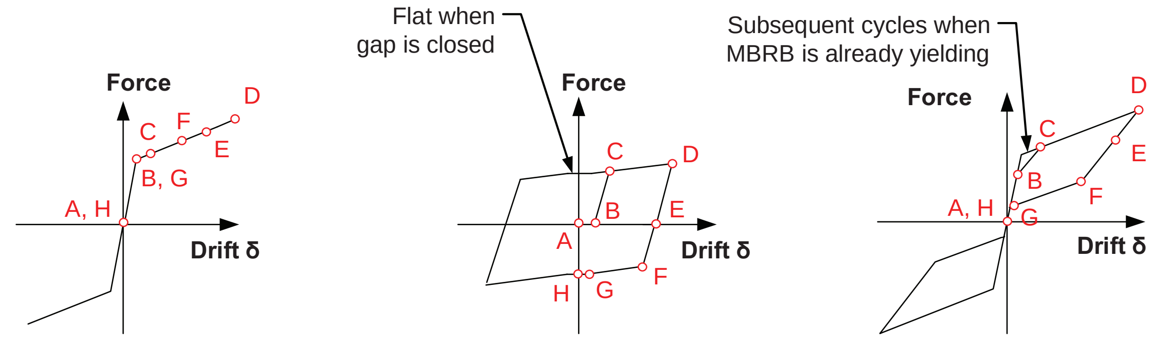

(a) Post-Tensioned beam *(b) MBRB* *(c) SCB*

A: Starting of the loading
B: Gap opening
C: Fuse yielding
D: Load reversal
E: Zero-force in the MBRB
F: Fuse yields in opposite direction
G: Gap closes
H: End of loading in one direction (near zero drifts)

Fig. 2. Schematic representation of the expected global response of an SCB moment frame.

shear forces, V, at the ends of the SCB are associated with lateral loading in the Figure 3 free-body diagram, but would include gravity loading in real structures.

From global equilibrium of horizontal forces on the assembled SCB, it can be shown that the horizontal reactions at the top of the SCB must be equal to the horizontal reactions at the bottom of the SCB acting in the opposite direction:

$$F_{IL} + F_{IR} = F_{TL} + F_{TR} \tag{1}$$

The moment at the left end of the SCB, M_L, can be defined as the average of the reactions at the left end, F_{TL} and F_{IL}, multiplied by the effective depth of the SCB, d_{SCB}, and the moment at the right end of the SCB, M_R, can be defined similarly. The sum of the moments at the two ends, $M_L + M_R$, can then be expressed as the sum of the top reaction forces multiplied by the depth of the SCB as given in Equation 2. The sum of the end moments could alternatively be expressed as the sum of the bottom reaction forces multiplied by the depth of the SCB, but top reaction forces are selected to facilitate the next step.

$$M_L + M_R = \left(F_{TL} + F_{TR}\right) d_{SCB} \tag{2}$$

From equilibrium of the top part of the SCB shown in Figure 3, the sum of the top reaction forces is equal to the PT force and MBRB force as given by:

$$F_{TL} + F_{TR} = F_{PT} + F_{fuse} \tag{3}$$

Substituting Equation 3 into Equation 2 results in the following equation describing the total moment of the SCB:

$$M_L + M_R = \left(F_{PT} + F_{fuse}\right) d_{SCB} \tag{4}$$

Equation 4 demonstrates that, unlike conventional moment frames, the moments at the two ends are inextricably linked. Stated a different way, there is not a unique combination of end moments, M_L and M_R, that satisfy equilibrium, nor do the two end moments need to be equal. For this reason, it is necessary to define a variable that describes the total flexural strength, M_n, as the sum of the two end moments, which is unique:

$$M_n = \left(F_{PTi} + F_{fuse}\right) d_{SCB} \tag{5}$$

where F_{PTi} is the initial post-tensioning force. It is convenient to express the total flexural strength, M_n, as a sum of two contributing moments, a moment associated with the initial post-tensioning force, M_{PTi}, and a moment associated with the MBRBs, M_{fuse}:

$$M_n = M_{PTi} + M_{fuse} \tag{6}$$

The force in the post-tensioning strands is the initial force plus the force due to additional post–gap-opening elongation. Because the primary interest here is flexural strength at initial gap opening and MBRB yield, the additional PT force due to post–gap-opening elongation is neglected. The moment due to initial post-tensioning force, M_{PTi}, and the MBRB yield force, M_{fuse}, are therefore given by the following:

$$M_{PTi} = A_{PT} \alpha_{PTi} f_{uPT} d_{SCB} \tag{7}$$

$$M_{fuse} = A_{ED} f_{yED} d_{SCB} \tag{8}$$

where A_{PT} is the total cross-sectional area of the post-tensioning strands, α_{PTi} is the ratio of initial post-tensioning stress to ultimate stress, f_{uPT} is the ultimate stress of the post-tensioning strands, A_{ED} is the total cross-sectional area of the MBRB cores, f_{yED} is the yield stress of the MBRB core plate, and d_{SCB} is the effective depth of the SCB as shown in Figure 1.

An important design parameter for any self-centering system is the measure of self-centering capability. In this study, the self-centering capability is defined by the variable α_{SC}, which is the ratio of restoring moment, M_{PTi}, to the moment that is resisting self-centering, M_{fuse}, given in Equation 9. If the self-centering ratio, α_{SC}, is greater than unity, then the system is expected to return to near zero drift when the lateral loads are removed.

$$\alpha_{SC} = \frac{M_{PTi}}{M_{fuse}} = \frac{A_{PT} \alpha_{PTi} f_{uPT}}{A_{ED} f_{yED}} \tag{9}$$

Two more equations that are useful in designing the SCB and understanding its behavior involve predicting the story drift ratios associated with post-tensioning strand yielding, $\gamma_{PT,y}$, and fracture of the MBRB, $\gamma_{fuse,fr}$. If the PT strain at yield is assumed equal to 0.01 in./in. to be consistent with ASTM A416 (ASTM, 2005), then the story drift ratio at PT yield can be expressed by Equation 10. Similarly, if a limiting average strain for fracture of the MBRB core is defined, $\varepsilon_{fuse,Lim}$, and the length of the MBRB core is given as L_{core}, then the limiting drift ratio for fuse fracture, $\gamma_{fuse,fr}$, can be expressed by Equation 11.

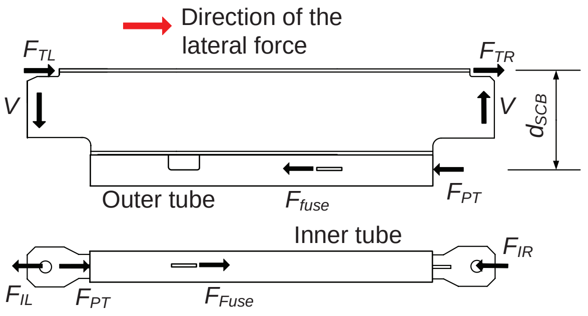

Fig. 3. Free-body diagram of an SCB (after gap opening).

Table 1. Test Matrix for Self-Centering Beam Experimental Program

SCB	SCB Depth, d_{SCB} (in.)	Fuse Core Area, A_{ED} (in.^{2})	Fuse Yield Force* (kips)	PT Diameter (in.)	Total PT Area, A_{PT} (in.^{2})	PT Stress Ratio, α_{PTi}	Initial PT Force (kips)	Self-Centering Ratio, α_{SC}	Flexural Strength, M_n (kip-ft)	Predicted Drift at PT yield, $\gamma_{PT,y}$ (%)
1	17.0	1.07	67.0	0.5	0.612	0.41	70.0	1.05	195	6.50
2	17.0	1.42	89.0	0.6	0.868	0.69	163	1.82	357	3.80
3	24.5	1.42	89.0	0.6	0.868	0.38	89.0	1.00	364	4.90
4	24.5	1.12	71.0	0.5	0.612	0.69	114	1.62	377	2.70
5	24.5	0.98	62.0	0.6	0.868	0.33	77.0	1.38	284	5.20

* The yield strength was calculated based on the measured yield stress of 62.8 ksi.

$$\gamma_{PT,y} = \frac{0.01\,L_{PT}}{d_{SCB}}\left(1-\alpha_{PTi}\right) \tag{10}$$

$$\gamma_{fuse,fr} = \frac{\varepsilon_{fuse,Lim}\,L_{core}}{d_{SCB}} \tag{11}$$

The effectiveness of the equations presented in this section for predicting behavior of the SCB will be evaluated against experimental results in subsequent sections. However, with the aid of these equations, it is possible at this point to conceptualize a design procedure. The design goals for the SCB are to have sufficient stiffness and strength (M_n) required for the specific application while maintaining a desired level of self-centering capability (α_{SC}) and deformation capacity. The following design procedure can produce an SCB that satisfies these design goals:

1. The section sizes for the SCB body (including the W-shape and two concentric tubes) can be selected to provide sufficient stiffness (Maurya, 2016).
2. Then, the moment associated with the post-tensioning, M_{PTi}, and the MBRBs, M_{fuse}, can be found by simultaneously solving Equation 6 and Equation 9 using the required flexural strength and desired self-centering ratio.
3. Combinations of the post-tensioning area and initial stress can then be checked using Equation 7 and Equation 10 to provide the required post-tensioning moment, M_{PTi}, while not yielding the strands at the desired design drift.
4. Finally, the MBRB core area and length can be found to produce sufficient flexural strength, M_{fuse}, using Equation 8, while limiting the strain as necessary using Equation 11.

EXPERIMENTAL PROGRAM DETAILS

A large-scale testing program was conducted at the Thomas M. Murray Structural Engineering Laboratory at Virginia Tech to validate the concept of the SCB, evaluate the efficacy of the design equations presented in the previous section, and investigate the effectiveness of the detailing. This section describes the experimental program, including test matrix, test setup, instrumentation, and construction process.

Test Matrix

The matrix of test specimens is presented in Table 1, including design details such as depth, d_{SCB}, MBRB core area, A_{ED}, and total area of PT strands, A_{PT}, as well as behavior-related design parameters such as flexural strength, M_n, self-centering ratio, α_{SC}, and predicted drift associated with PT yielding, $\gamma_{PT,y}$, calculated using Equations 6, 9, and 10, respectively.

The testing program was designed to strategically vary the design parameters. The SCB are approximately two-thirds scale relative to the beams in a three-story prototype building described by Gupta and Krawinkler (1999). The flexural strength, M_n, of the SCBs varied between 195 kip-ft to 377 kip-ft, which represents the range of total moment demand (sum of the two end moments) in the prototype building moment frame beams as scaled for similitude to the two-thirds scale. See Maurya (2016) for additional details. The self-centering ratio, α_{SC}, is another key design variable that affects system behavior and was varied from 1.00 to 1.82. SCBs with lower values of self-centering ratio are expected to lose their ability to eliminate residual drift after some PT seating losses and strain-hardening in the fuse. Conversely, the larger values of self-centering ratios are expected to enforce minimal residual drift but exhibit less energy dissipation. To examine the effect of post-tensioning yield and fracture on the behavior of the SCB system, the predicted story drift associated with PT yield was varied from 2.7% to 6.5%, which results in an initial PT stress between 33% and 69% of the PT ultimate strength. SCB specimens with small expected drift at PT yield were included to investigate PT related limit states (i.e., yield and fracture), while SCB specimens designed to delay PT yield demonstrate that the SCB can be designed to create exceptionally large ductility and deformation capacity.

To achieve the desired variations discussed here and listed in Table 1, two SCB assemblies were built with depths d_{SCB} = 17 in. and d_{SCB} = 24.5 in. The five SCB specimens were created by replacing the post-tensioning strands and MBRB components, but the two SCB assemblies (i.e., beams, tubes, and connections) were reused for all tests and showed no permanent damage.

Detailing and Fabrication of the SCB

The SCB was detailed with end plate connections to the column that were easily removable and connections to the end plate that allow damage-free rotation up to large story drifts. Because of detailing choices like these used to facilitate the test program, the resulting SCB may not be commercially competitive in its current form due to related cost and complexity. However, the detailing of the SCB could be streamlined to make it more efficient and economical in the future. Additional details about the SCB detailing and construction can be found in Maurya (2016).

The SCB detailing is shown in Figure 4, and Figure 5 shows pictures of specimen SCB 2. The ends of the tubes as well as the bottom flange of the I-shaped beam were machined to have equal length. The top wall of the outer tube was removed as shown in Figure 4(c) to allow assembly. The inner tube with the cruciform end connection pieces and sliding anchorage plates already attached was laid inside the outer tube before the outer tube was welded to the bottom flange of the I-shaped beam. Before assembly, greased plastic spacers were attached to the surface of the inner tube on all four faces and at four locations along the length to keep the inner tube centered in the outer tube. The thickness of the spacers was selected to produce a tight fit against the inside of the outer tube.

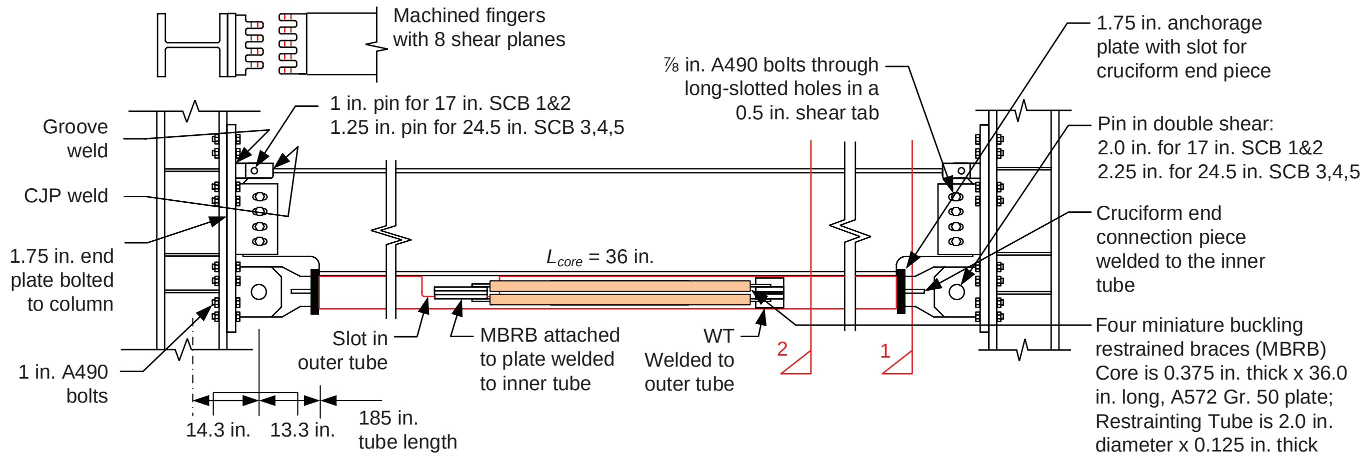

(a) Side view

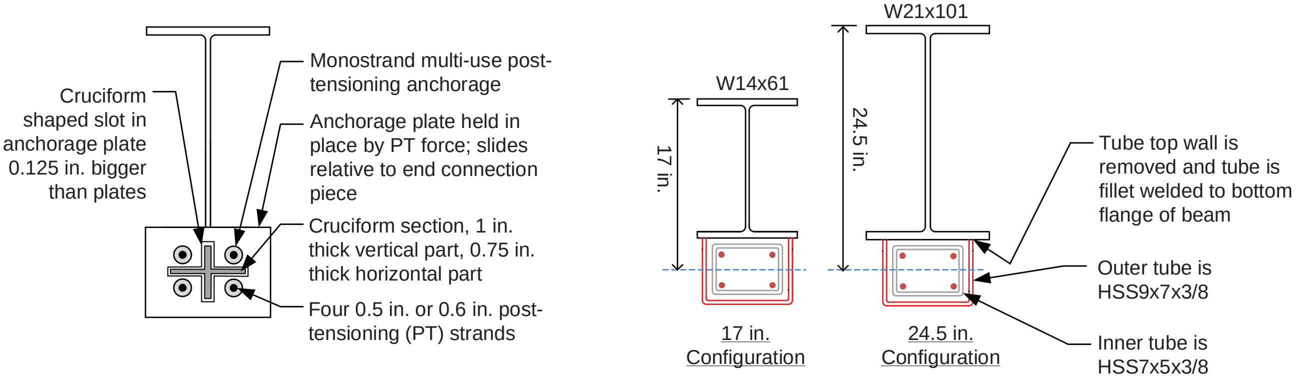

(b) Section 1 at anchorage plate *(c) Section 2 at SCB cross section*

Fig. 4. Selected construction details.

Post-tensioning strands were then threaded through the inner tube. The PT stressing operation was conducted with the SCB lying flat on the floor and was done before the end plates were installed on the ends. A multi-use, mono-strand chuck anchorage system was used as pictured in Figures 5(b) and 5(c). As shown in Figure 5(b), a load cell (blue) was placed under the chuck at the left ends and as shown in Figure 5(c), a steel spacer (red) was placed under the chuck at the right end to facilitate easy removal of the post-tensioning strands. Procedures described by Bruce (2014) were used to calculate the proper jacking force to apply that would result in the target PT force after seating losses. Seating losses are associated with wedge displacement into the chuck body when the jacking force is removed. In most cases, the PT forces achieved in each strand were within 5% of the target PT forces.

The connection at the top and bottom flanges to the end plate were designed with a true pin and detailed to be vertically aligned with each other and horizontally aligned with the center of the flange at the top and center of tube at the bottom. As shown in Figure 4(a), the pin at the top flange is part of a finger joint that has eight shear planes while the pin at the bottom flange is a large-diameter (2.0 in. or 2.25 in.) pin in double shear. The tolerance in the pin holes has an effect on the stiffness and load-deformation behavior of the SCB, and therefore it is desirable to make the tolerance as small as possible; a tolerance of $\frac{1}{40}$ in. was selected to be as small as possible while large enough to allow relatively easy assembly. The shear connection between the SCB and the end plate was accomplished with $\frac{7}{8}$-in.-diameter bolts in slotted holes. The shear bolts were finger tightened and thus

(a) Overall view

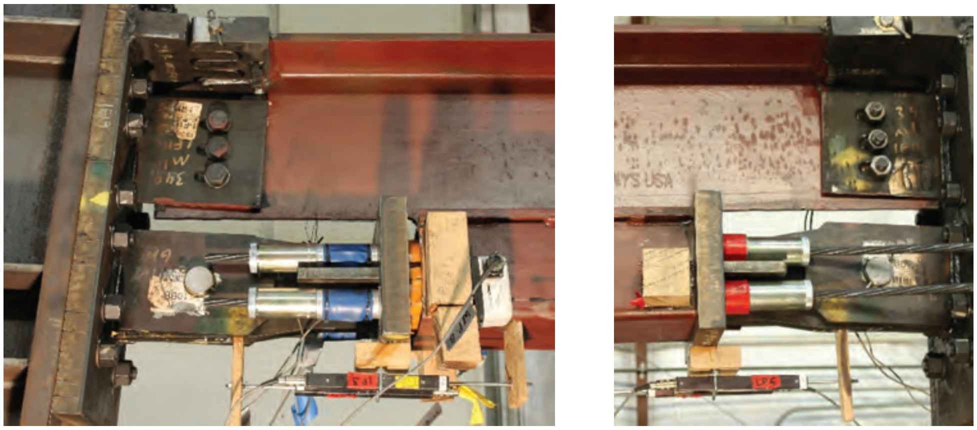

(b) Left-end connection

(c) Right-end connection

Fig. 5. Pictutre of specimen SCB 2 at 6% story drift.

allowed SCB end rotation without any damage. At this stage of construction, the SCB can then be bolted to the columns.

The miniature buckling restrained braces (MBRBs) are small-capacity, buckling restrained braces that were specifically designed and developed to produce the yield strength and deformation capacity needed for the SCB (Maurya et al., 2016). With a core plate that is ⅜ in. thick and a restraining tube that is 2 in. in diameter, the MBRBs are smaller than commercially available buckling restrained braces. The study by Maurya et al. (2016) determined the proper proportioning and detailing necessary to avoid buckling and create full hysteretic behavior up to average core strains of 3.5% during fully reversed cyclic loading. The core plate geometry for the MBRBs used in this study have a thickness of ⅜ in. with a width equal to 0.71 in., 0.94 in., 0.94 in., 0.74 in., and 0.65 in. for SCB1 through SCB5, respectively. Maurya et al. (2016) found that smaller aspect ratios are more susceptible to early fracture, and the aspect ratios used in this study (1.7 to 2.5) are representative of MBRBs that were capable of sustaining large inelastic strains in Maurya et al. (2016).

A total of four MBRBs were used in each specimen as shown in Figures 4(a) and 5(a) to produce a symmetric configuration with a center point coincident with the center of the tubes. One end of the MBRB [the left side in Figure 4(a)] was attached to a wing plate that passed through a slot in the outer tube and welded to the inner tube, while the other end was attached to a WT that was welded to the outer tube. In this way, the MBRB was subjected to axial deformation as the inner and outer tubes experienced relative movement (telescoping). The attachment at the ends of the MBRB was accomplished by welding the core plate to a connection plate that was, in turn, bolted to the wing plate or WT stem, thus allowing easy replacement between tests.

Material Properties

The materials used for the SCB were as follows: I-shaped beam, ASTM A992; tubes, A500 Gr. B; pins, Gr. 1554; plates, ASTM A572 Gr. 50; post-tensioning strands, ASTM A416; MBRB core plate, ASTM A572 Gr. 50; and welds, E70 electrodes. Measured properties of the MBRB core plate were obtained from two coupons as described in Maurya et al. (2016). The resulting material properties were yield stress equal to 62.8 ksi, ultimate strength equal to 81.1 ksi, and a maximum elongation of 26%.

The nominal ultimate strength for the post-tensioning strands is 270 ksi, and the measured material properties based on five tests of each diameter were yield stress F_y = 257 ksi, ultimate strength F_u = 296 ksi, and modulus of elasticity E = 28,900 ksi for 13-mm-diameter strands and F_y = 256 ksi, F_u = 291 ksi, and E = 28,900 ksi for 15-mm-diameter strands. The yield stress was taken as the stress at 1% strain as specified in ASTM A416 (ASTM, 2005). Bruce and Eatherton (2016) describe a detailed study on the behavior of the post-tensioning strand material and the PT system behavior (with anchorage) with the same material and anchorage used in the SCB. The work by Bruce and Eatherton (2016) includes characterization of the PT material, seating losses during stress transfer, seating losses during cyclic loading, strain at initial wire fracture, progression of wire fracture, and ductility in the PT system.

Test Setup, Instrumentation, and Displacement Protocol

The test setup is shown in Figure 6 and consists of a one-bay SCB moment frame with a 240-in. distance between column centerlines and a 104-in. height from column base pin to actuator force. The height of the column simulates the idealized height between inflection points in the prototype building column when the moment frame is subjected to lateral loading. It was necessary to test a full bay moment frame, as opposed to a single-sided moment connection test, because the post-tensioning extends the full length of the SCB, and the flexural strength of the SCB is the sum of the moments produced at the two ends as described by Equation 4. Downward force was applied at the third points of the SCB to simulate the gravity loads coming from two intersecting beams that would be supported by the SCB in the prototype building. Based on the tributary area of the intersecting beams, the assumed dead and live loading given for the prototype building, and a load case with full dead load and 25% of the live load, a gravity force of 11.9 kips was calculated. See Maurya (2016) for additional details. The SCB was laterally braced at these same locations to simulate the lateral restraint provided by the intersecting beams and also the columns were laterally braced at the height of the actuator.

Some of the instrumentation is shown in Figure 6, including (1) six wire potentiometers that measured lateral translation of the columns, (2) four linear potentiometers that measured the gap openings at the ends of the tubes, (3) two wire potentiometers that measured the axial deformation of the MBRBs, and (4) four inclinometers used to measure the drift angle of the columns and rotation of the SCB ends. In addition to the instrumentation shown in Figure 6, the following instrumentation was also included: (1) load cells on every PT strand as shown in Figure 5(b), (2) four load cells to monitor the gravity force, (3) load and displacement from the actuator, and (4) approximately 50 strain gages. The strain gages were arranged in strain-gaged sections where a group of 18 strain gages were used to capture the average axial strain, major axis curvature, and minor axis curvature in the SCB at three locations along its length. Because the SCB body remained elastic, this allowed the calculation of axial force in the SCB at each of the three locations and, in turn, the axial force in the MBRBs.

The reversed cyclic displacement protocol specified in the

AISC *Seismic Provisions* (AISC, 2016) for qualification of special moment frames was used up to 6% story drift, at which point the specimen was subjected to repeated cycles at 6% story drift until the MBRB or PT fractured. It is noted that 6% story drift is on the upper end of what is expected for a self-centering moment frame subjected to a maximum considered earthquake ground motion (Lin et al., 2013). The loading rate was 2 in./min for the first 18 cycles (0.375%, 0.5%, and 0.75% story drift cycles) and 3 in./min for the rest of the test.

EXPERIMENTAL RESULTS

Several aspects of the SCB test results were analyzed to evaluate the performance of the overall SCB, behavior of the components, and efficacy of the proposed design equation. This section is organized into the following parts: (1) self-centering capability, (2) stiffness of the SCB, (3) flexural strength of the SCB, (4) deformation capacity, (5) behavior of the restoring force mechanism, and (6) MBRB behavior.

Self-Centering Capability

The global load-displacement behavior of the SCB specimens is shown in Figure 7. The vertical axis is normalized moment, which is the measured actuator force multiplied by the story height, $h = 104$ in. (see Figure 6) and divided by the predicted flexural strength, M_n, as calculated using Equation 6 and given in Figure 7 and Table 1. The horizontal axis is the horizontal story drift measured using WP-1 (see Figure 6) divided by the same story height, h.

The load-displacement behavior of all five SCB specimens exhibited the expected flag-shaped hysteresis loops that return to near-zero story drift when the applied lateral force is removed. For SCB specimens with low self-centering ratios (i.e., α_{SC} near 1.0 like specimens SCB 1 and SCB 3), the drift at zero force stays negligible through cycles up to 2% or 3% story drift. Strain hardening in the MBRB core and losses in the post-tensioning strand stress due to anchorage wedge seating, strand yielding, and wire fracture lead to increasing drifts at zero force.

Table 2 tabulates the average residual story drift ratio after the lateral force was removed (average of positive and negative excursions) during the first cycle at 2% and 4% story drift. Specimen SCB 3, with a small self-centering ratio, $\alpha_{SC} = 1.0$, exhibited negligible drifts of 0.11% at zero force during the cycles at 2% story drift but, during larger cycles up to 4% story drift, lost the ability to eliminate residual drifts and experienced story drifts of 1.3% when the lateral load was removed.

Conversely, specimen SCB 2 had a self-centering ratio, $\alpha_{SC} = 1.82$, and exhibited negligible drift at zero force through the 4% story drift cycles (0.14%) and throughout the test up to and including cycles at 6% story drift. Specimen SCB 4 had a large self-centering ratio of $\alpha_{SC} = 1.62$, but because the initial post-tensioning stress was high, $\alpha_{PTi} = 0.69$, the post-tensioning strands had individual wires fracture, which led to loss of post-tensioning force and an increase in the drift at zero force up to 0.84% during the 4% story drift cycle.

While the drift at zero force is an adequate measure of the maximum possible residual drift that can occur if the lateral load is slowly removed after an excursion to the peak drift, the actual residual drifts during an earthquake are expected to be much smaller (Eatherton and Hajjar, 2011; Eatherton et al., 2014). Self-centering seismic force-resisting systems that can eliminate, or reduce to negligible magnitude, the story

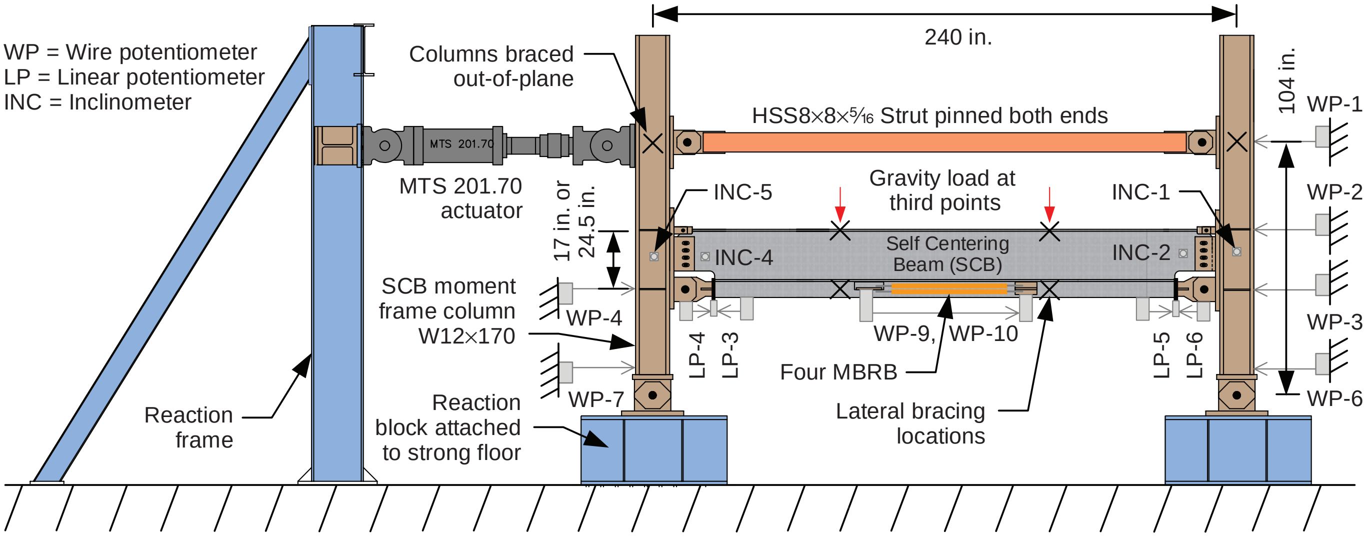

Fig. 6. Self-centering beam test setup and instrumentation.

Table 2. Selected Experimental Results

SCB	SC Ratio	Drift at Zero Force*	Drift at Zero Force**	Initial Stiffness (kip/in.)	Post–Gap-Opening Stiffness (kip/in.)	Story Drift at Fuse Yield	Story Drift at PT Yield, $\gamma_{PT,y}$	Predicted Drift at PT Yield	Ratio of Measured $\gamma_{PT,y}$ to Predicted
1	1.05	0.08%	0.31%	31.0	4.00	0.64%	—	6.5%	—
2	1.82	0.06%	0.14%	48.0	5.60	0.71%	4.6%	3.8%	1.21
3	1.00	0.11%	1.30%	78.0	11.7	0.40%	5.1%	4.9%	1.04
4	1.62	0.14%	0.84%	79.0	9.00	0.45%	3.1%	2.7%	1.15
5	1.38	0.16%	0.70%	64.0	11.7	0.40%	—	5.2%	—

* Taken during 2% story drift cycles
** Taken during 4% story drift cycles

drift after lateral load is removed are sometimes referred to as having full self-centering capability. However, previous studies on self-centering systems have proven that full self-centering is not required to reliably eliminate residual drifts. Nonlinear response history analyses on numerous prototype buildings have shown that self-centering ratios as low as $\alpha_{SC} = 0.50$ result in near-zero residual drifts after design earthquakes (Eatherton and Hajjar, 2011; Eatherton et al., 2014; Eatherton and Maurya, 2018). Even though the hysteretic behavior does not explicitly eliminate the possibility of residual drifts, if there is some restoring force present then there is an increased probability for yielding toward zero drift after large-story drift excursions. This creates a propensity to shake down to near-zero residual drift during the earthquake, which has been referred to as probabilistic self-centering (Eatherton and Hajjar, 2011).

Stiffness of the SCB

The initial stiffness and post–gap-opening stiffness of the SCB specimens is summarized in Table 2. As expected, specimens SCB 1 and SCB 2, which had a shallower depth and smaller steel section [see Figure 4(c)], exhibited smaller initial stiffness than the other three specimens. Perhaps less intuitive is the dependence of the initial stiffness on the post-tensioning force, which can be observed by comparing the initial stiffness of SCB 1 and SCB 2. SCB 2 had the same steel section as SCB 1, but a larger post-tensioning force by a factor of 2.33 and exhibited 56% larger stiffness. It might be expected that before gap opening, the SCB would have a stiffness equivalent to a moment frame for which the anchorage plates are rigidly attached (e.g., welded) to the ends of both tubes. In this case, the initial stiffness would be identical for specimens with the same steel section. The theoretical stiffness of the SCB specimens was derived based on this assumption (Maurya, 2016) to be 167 kip/ft and 328 kip/ft for the smaller SCB (specimens SCB 1 and SCB 2) and the larger SCB (specimens SCB 3, SCB 4, and SCB 5), respectively. The initial stiffnesses given in Table 2 are between 3 and 5 times smaller than the theoretical stiffness and have a clear correlation to the post-tensioning force.

To gain some understanding of the SCB initial stiffness, an excerpt of the results for specimen SCB 1 is investigated in Figure 8. The gap-opening ratio (vertical axis) is a measure of the rotation angle at the end of the SCB. If the gap-opening mechanism were perfect (i.e., gaps open at both ends instantaneously) and there was no increase in lateral loads after gap opening (i.e., no MBRBs or increase in post-tensioning force), then the idealized gap opening versus story drift response would be exactly zero until the applied moment reached the post-tensioning moment, M_{PTi}, and then the slope would sharply change to unity. Figure 8 shows that the gap opening behaves more like a gradual progression.

The inner and outer tubes were saw cut to be nominally the same length and then a grinder was used to smooth out the surface, but the bearing surfaces were not perfectly flat nor perfectly even with each other. It is estimated that the lengths of the two tubes and the I-shaped beam were all within 1⁄32 in. of each other. However, because the inner and outer tubes have different areas and thus different axial stiffness, even if they are exactly the same length, they do not equally share the post-tensioning axial load. As a result of imperfections and the difference in axial stiffness, the gap-opening joint is not perfectly rigid prior to gap opening, and this flexibility is observed as the nonzero initial part of the slope in Figure 8. The slope of the initial gap-opening ratio of 0.18 relative to the story drift ratio is approximately 20% of the post–gap-opening slope and, thus, is contributing to a significant reduction in the initial stiffness of the SCB. This also explains the dependence of the initial stiffness on post-tensioning force because the gap-opening joint becomes more rigid because there is more clamping force applied by the post-tensioning.

Maurya (2016) calibrated a set of equations to predict the stiffness of the SCB in which the post-tensioning force is used to determine how close the initial stiffness is to the upper bound (stiffness assuming a rigidly closed gap-opening joint) or the lower bound (the post gap-opening stiffness). Maurya further developed a procedure to calculate an equivalent moment of inertia that could be used in simple elastic models during design. However, it is expected that higher initial stiffness of the SCB system could be obtained by (1) machining the tubes, I-shaped beam, and anchorage plates to have tighter tolerances for length and flatness and (2) using tubes that have the same area.

Flexural Strength of the SCB

The measured flexural strength was determined as the intersection of two lines fit to the initial stiffness and the post–gap-opening stiffness, and the resulting values are given in Table 3. As shown in Table 3, the predicted flexural strength calculated using Equation 6 was between 1% unconservative for specimen SCB 2 and 12% conservative for specimen SCB 1, with an average error of 5% on the conservative side relative to the measured flexural strength. The predicted

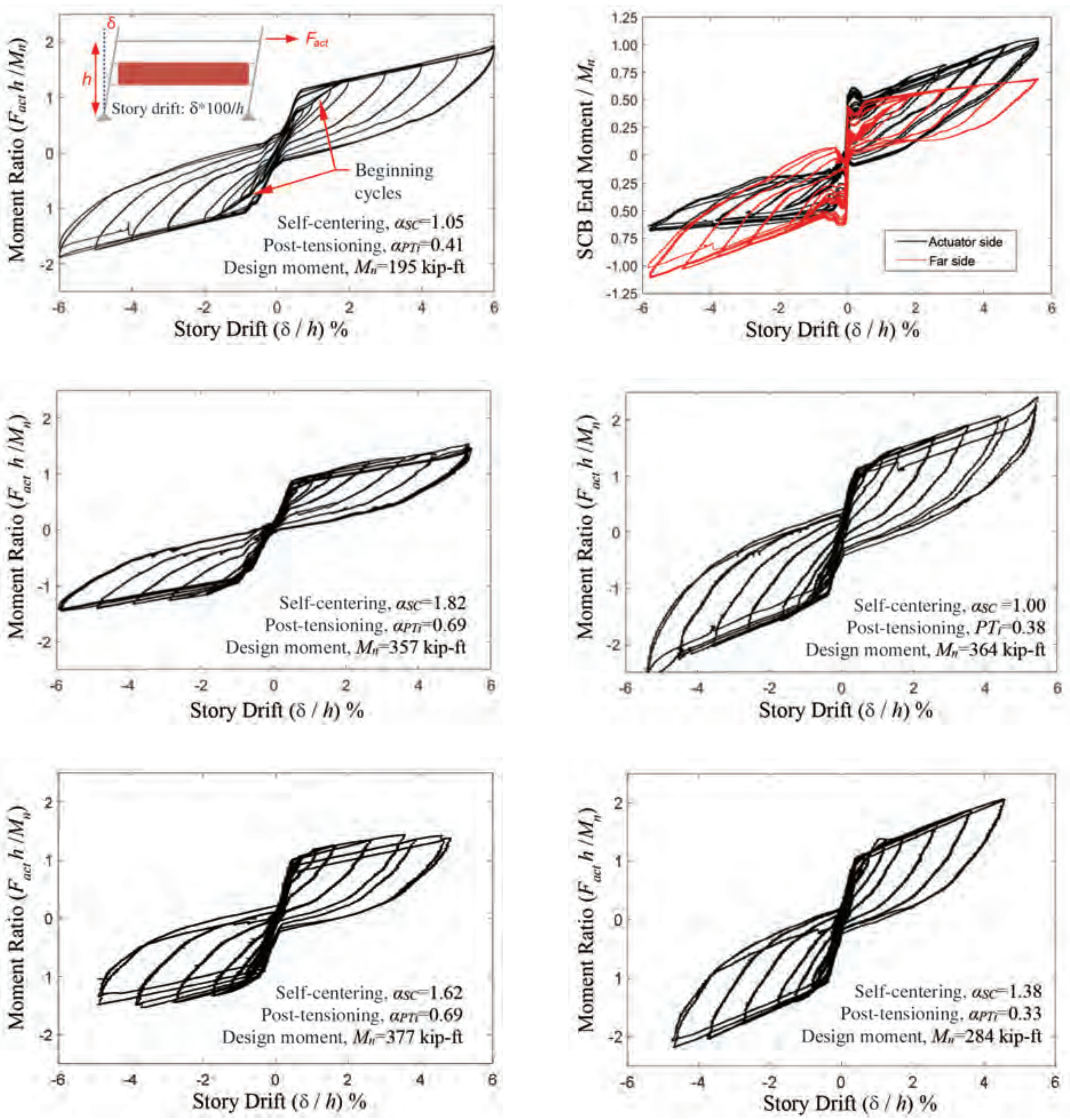

Fig. 7. Hysteretic behavior of self-centering beams.

Table 3. Comparison of Predicted and Measured Behavior						
SCB	Predicted Flexural Strength, M_n (kip-ft)	Measured Flexural Strength (kip-ft)	Ratio of Measured M_n to Predicted	Predicted M_{PTi} (kip-ft)	Measured M_{PTi} (kip-ft)	Ratio of Measured M_{pti} to Predicted
1	195	219	1.12	99.0	107	1.08
2	357	352	0.99	230	234	1.02
3	364	366	1.00	182	198	1.09
4	377	393	1.04	233	250	1.07
5	284	302	1.06	158	174	1.10

flexural strength will tend toward conservative because the prediction is based on the initial post-tensioning force, but the post-tensioning strands experience additional elongation and force by the time the MBRBs yield.

As predicted in Figure 2(c), the beginning cycles exhibited a change in stiffness (i.e., softening) before reaching the flexural strength, M_n [e.g., see Figure 7(a) for SCB 1]. Subsequent cycles, after the MBRBs have yielded, reach M_n without softening and fill out the corner of the flag shape. This effect was most pronounced for specimen SCB 1 and was minor for other specimens.

As discussed previously, the predicted flexural strength, measured flexural strength, and the vertical axes in Figure 7 are all based on total moment, which is the sum of the moments at the two ends of the SCB. Figure 7(b) examines the distribution of moment between the two ends and was obtained from a strain-gaged cross section on each end of the SCB. Figure 7(b) shows that prior to gap opening, the moments at the two ends are similar, and during gap opening, there is a shifting of moments back and forth.

After gap opening, there is a steady trend wherein the actuator side takes larger moments during positive excursions and the far side experiences larger moments during negative drift excursions. This can be explained by examining the free-body diagram of Figure 3, which could be viewed as showing positive story drift if the actuator side is on the left. The post-tensioning force, F_{PT}, is applied to the inner tube at the left end, which corresponds to the actuator end. Because the post-tensioning force is closer to the actuator side, it contributes to a larger reaction, F_{IL}, at the actuator side and a smaller force, F_{IR}, at the far side. Thus, the corresponding moment is larger at the actuator side and smaller at the far side for positive story drift. At the peak drift, the larger end moment is as much as 60% larger than the smaller end moment. This difference in SCB end moments and the peak moment that is likely to occur at one end of the SCB should be considered in the design of the columns. A computational study examining the distribution of moment between the two beam ends is presented in by Huang et al. (2017) and design recommendations are presented by Maurya (2016).

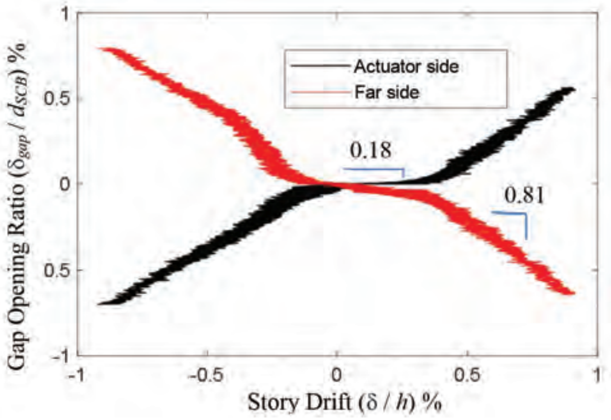

Fig. 8. Gap-opening behavior for SCB 1.

Deformation Capacity

Figure 7 shows that the SCB moment frame has exceptionally large deformation capacity. All SCB specimens were subjected to cycles up to 5% or 6% story drift, and there was no observable damage to the I-shaped beam, tubes, anchorage plates, or connections. Strain gages confirmed that the steel shapes that comprise the SCB remained elastic. Inelastic damage was confined to the MBRBs and the post-tensioning. Because the test setup was limited to 6% story drift, some specimens were subjected to multiple cycles at 6% and were stopped only when there was fracture of the post-tensioning strands or fracture of the MBRBs.

The deformation capacity of the SCB can be controlled in the design process using Equations 10 and 11. The story drift at which post-tensioning yield is expected is shown in Equation 10 to be a function of the post-tensioning strand length, L_{PT}, divided by the depth of the SCB, d_{SCB}, and the post-tensioning stress ratio, α_{PTi}. Selecting a larger ratio, L_{PT}/d_{SCB}, or a smaller value for α_{PTi} leads to larger story drifts before post-tensioning yield. Similarly, Equation 11 shows that fracture of the MBRBs is a function of the ratio of the core length, L_{core}, to the depth of the SCB, d_{SCB}. Longer MBRB cores (i.e., larger ratios of L_{core}/d_{SCB}) lead to larger deformation capacity before MBRB fracture. It is possible to design SCB configurations with drift capacity well in excess of 6% story drift before undesirable limit states occur.

Table 2 summarizes the story drift associated with fuse (i.e., MBRB) yield and post-tensioning yield. The story drift at fuse yield was determined as the point when there was significant change in stiffness in the MBRB component, whereas the story drift at post-tensioning yield was determined as the point when the post-tensioning strain reached 0.01 in./in. Table 2 shows that the prediction of story drift for post-tensioning yield using Equation 10 was between 4% and 21% smaller than the experimentally observed drift at post-tensioning yield. Equation 10 is derived assuming all components of the SCB behave as rigid bodies and the story drift ratio is equal to the gap-opening ratio. Although the flexibility of the SCB, column, and connections makes Equation 10 somewhat conservative, it is still deemed useful for design purposes.

One of the objectives of the SCB configuration, as compared to previously proposed self-centering moment frames, is to keep the columns the same distance apart so there is no deformation incompatibility between the SCB and diaphragm. By comparing the rotations measured from the inclinometers (INC-5 and INC-1 in Figure 6) and comparing the displacements of the two columns (WP-4 and WP-3 in Figure 6), it is possible to estimate the degree to which the columns are staying equidistant apart during large drift cycles. The rotations of the two columns were found to be nearly identical. The difference in the column displacements at the height of the SCB was found to be approximately ⅛ in. on average during excursions to 6% story drift. This difference in column displacements is likely due to pin hole tolerances and is found to be a negligible fraction of the length of the bay. Therefore, the hypothesis that the frame does not expand during lateral drift is verified.

Behavior of the Restoring Force Mechanism

The behavior of the restoring force mechanism is examined in Figure 9 with plots of the normalized PT moment versus the gap-opening ratio. The post-tensioning moment was found as the measured force in the PT strands multiplied by the depth of the SCB and normalized to the calculated initial post-tensioning moment using Equation 7 and listed for each specimen in Figure 9. The horizontal axes are the gap-opening ratio, which, as described previously, is the measured gap opening divided by the depth of the SCB.

Figure 9 clearly shows the expected bilinear elastic behavior described in Figure 2(a). The figure also shows that the predicted gap-opening moment, M_{PTi}, is fairly accurate at predicting the moment associated with decompression and gap opening because the stiffness changes occur at a moment ratio equal to unity. Table 3 summarizes the comparison of measured to predicted moment at gap opening and indicates the experiments produced a moment that was 7% larger than Equation 7 on average. The post–gap-opening stiffness is also relatively straightforward to predict and is a function of the PT area, length of PT strands, and the square of the SCB depth. The derivation of an equation for post–gap-opening stiffness and evaluation of the equation's accuracy is not included here, but details can be found in Maurya (2016).

A reduction in the post-tensioning moment is observed for all specimens in Figure 9 following large cycles of story drift. The effect is most pronounced in specimens with large initial post-tensioning stress ratios, α_{SC}, like specimen SCB 4. The losses in PT force are associated with seating losses, PT strand yielding, and fracture of individual wires in the seven-wire PT strands.

To understand the causes for losses in PT force, it is convenient to examine the average stress versus average strain behavior for the group of PT strands in specimens SCB 1 and SCB 4 as shown in Figure 10. The average stress is calculated as the total measured PT force in all strands divided by the nominal area and normalized to the nominal ultimate strength (taken as 270 ksi), while the average strain is calculated as the elongation of the PT strands (assumed to be equal to the measured gap opening) divided by the length of the strands between anchorages, which was 185 in. This calculation of average strain neglects the axial deformation of the tubes. As mentioned on Figure 10, specimen SCB 1 was stressed to 41% of the nominal ultimate strength, whereas specimen SCB 4 was stressed to 69% of ultimate, which leads to significantly larger total PT strains during testing and allows more exploration of PT-related limit states.

As shown in Figure 10, the PT strands in specimen SCB 1 exhibit some nonlinearity during cycles of stress between 0.4 and 0.8 times the ultimate strength. Because the peak stress in the strands was 93% of the ultimate strength, it is unlikely that the nonlinearity is due to inelasticity. Instead, most of this nonlinearity and associated loss in PT stress when the strain returns to its starting point is associated with seating losses. Seating losses for these types of PT strand systems were studied in detail and characterized by Bruce and Eatherton (2016). Seating losses occur when the wedges sink down into the conical barrel of the chuck anchorage when the strand is subjected to stresses greater than those previously experienced. Seating losses are not as important for design of prestressed concrete structures because the strands are typically stressed to levels close to the yield stress, and the strands are not subjected to large variations in stress. In self-centering seismic systems where the initial stresses may be small and the PT stress variations can be large during earthquake events, the effect of seating losses on self-centering capability may need to be considered. See Bruce and Eatherton (2016) and Maurya (2016) for details.

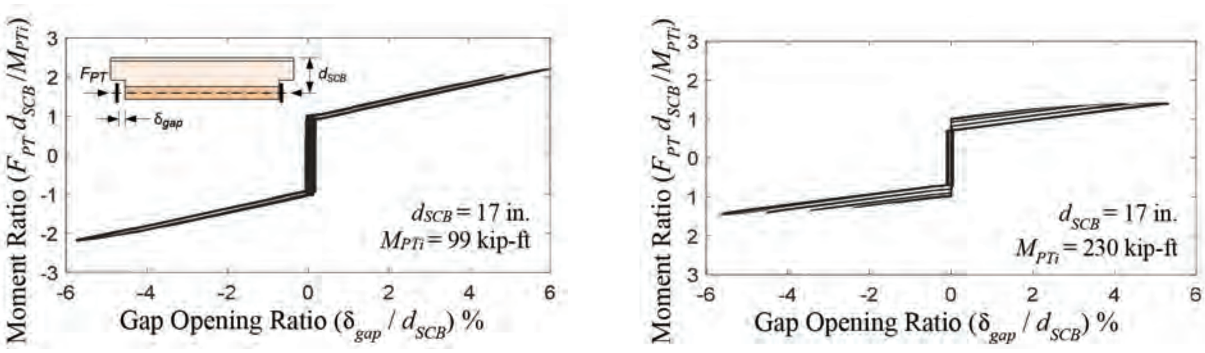

(a) Specimen SCB 1

(b) Specimen SCB 2

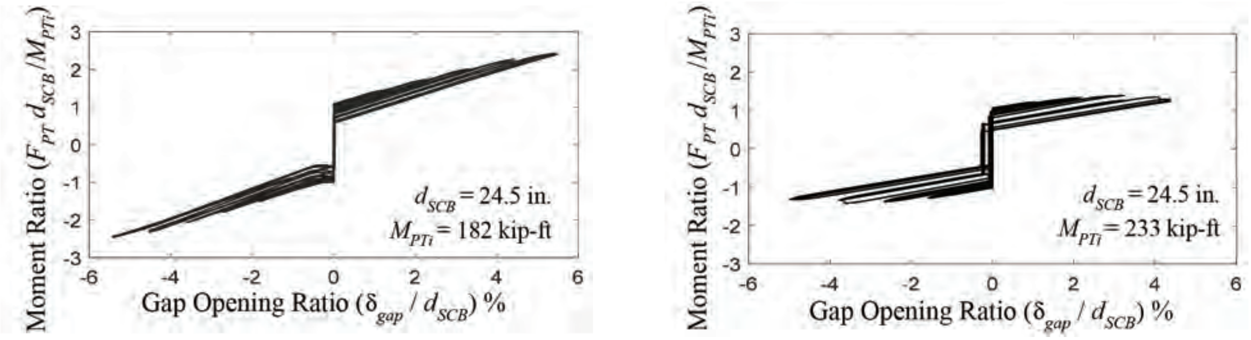

(c) Specimen SCB 3

(d) Specimen SCB 4

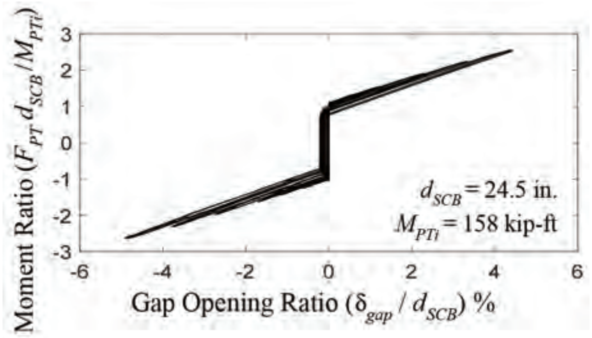

(e) Specimen SCB 5

Fig. 9. Isolated behavior of the restoring force system.

Specimen SCB 4, shown in Figure 10(b), demonstrates the behavior of the PT strands when subjected to large strains past yield. As the average strain passes 1% and the PT stress ratio exceeds 0.9, yielding of the PT strands is assumed to occur. At an average strain of 1.13%, one wire in one of the four PT strands fractured, and at 1.18% strain a wire in a different strand fractured. For each fracture, there was a reduction in the PT force of about 5% of the total load. The loss of two wires in the set of four PT strands, each consisting of seven wires, implies a small loss of PT area (2 out of 28 wires) and load-resisting capacity. Because of the mode of failure whereby individual wires fracture, the post-tensioning system has considerable redundancy.

For the other four specimens (other than specimen SCB 4), none of the PT strands experienced fracture while the average strains exceeded 1.2% in some cases. Bruce and Eatherton (2016) found that the average strain associated with first wire fracture was 2.3% with a standard deviation of 0.5% for the exact same PT strand and multi-use, chuck-style anchorage system used in this study (based on 12 specimens). The reason that specimen SCB 4 experienced unexpectedly early wire fracture was likely due to the fact that the post-tensioning anchorage was reseated on the same part of the strand during the stressing process. Reseating is when the pressure on the stressing jack is released, allowing the anchorage wedges to bite into the strand, but then the stressing jack is pressurized again and the chuck anchorage moved slightly before releasing the jack pressure a second time. Reseating the wedges on the same part of the strand causes damage to the PT strands and should not be allowed during the post-tensioning process.

Figure 10 shows that specimen SCB 1 experienced 11% loss of the initial PT force, and specimen SCB 4 lost 56% of its initial PT force as the specimens were cycled beyond 5% story drift. If self-centering capability after extreme story drifts is part of the performance goals of the SCB, these losses in PT force could be accounted for in design by calculating an effective self-centering ratio using Equation 9 with a reduction in the term $\alpha_{PTi} f_{uPT}$.

MBRB Behavior

The axial load versus deformation behavior of the MBRBs is shown in Figure 11. The MBRB force, F, was based on the difference in the inner tube force on either side of the MBRB connection as measured using strain gages. The vertical axes are normalized to the predicted MBRB strength, F_{fuse}, calculated as the measured yield stress multiplied by the area, which is reported in Figure 11 and tabulated in Table 1. The average core strain was calculated as the measured axial deformation of the MBRB, δ_{fuse}, divided by the core length, L_{core} = 36 in. It is noted that the measured axial deformation includes the elastic deformations of the end regions of the MBRB (outside the core), but this is not expected to cause significant error in the average core strain measurement.

In all five specimens, the MBRBs exhibited full and stable hysteretic behavior as shown in Figure 11. Because specimens SCB 1 and SCB 2 had a shallower depth (d_{SCB} = 17 in.) as compared to specimens SCB 3, SCB 4, and SCB 5 (d_{SCB} = 24.5 in.), the MBRBs did not experience as large axial deformations for the same magnitude of story drift. The MBRBs in specimen SCB 2 experienced the smallest axial deformations of approximately 2% average strain, in part because the bolted connections at the ends of the MBRB were slipping. For subsequent specimens, the bolts were fully pretensioned and did not experience sliding at the bolted connection.

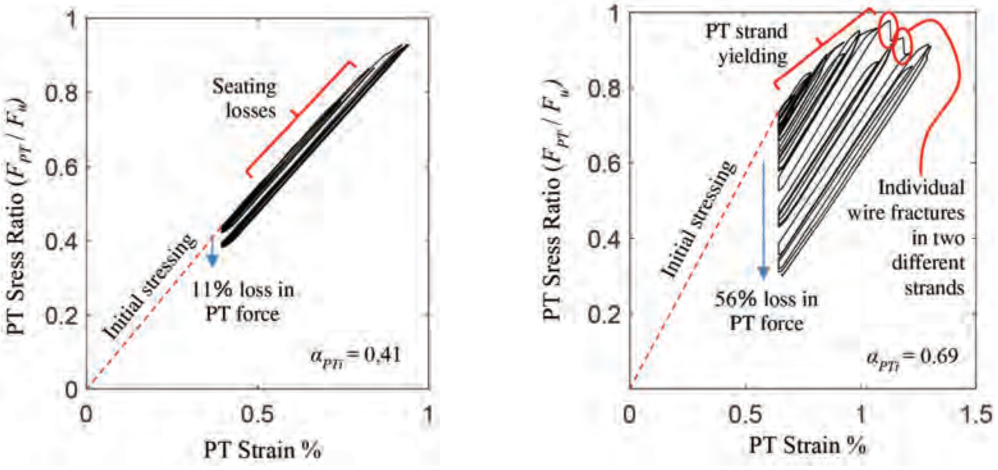

(a) Specimen SCB 1

(b) Specimen SCB 4

Fig. 10. Response of post-tensioning strands.

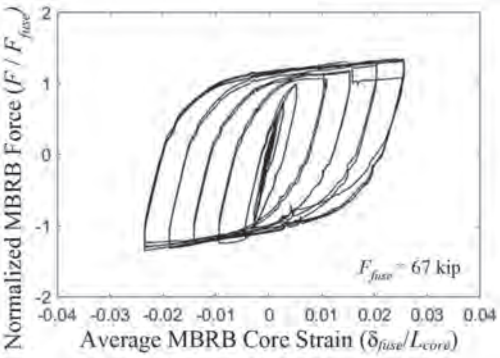

(a) MBRB behavior for SCB 1

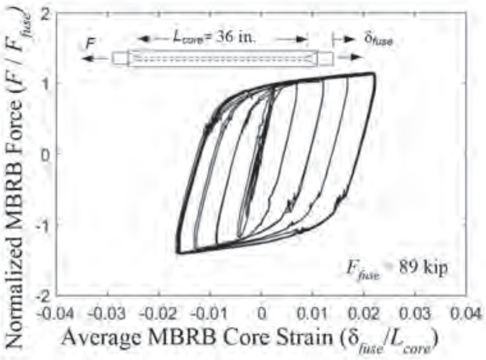

(b) MBRB behavior for SCB 2

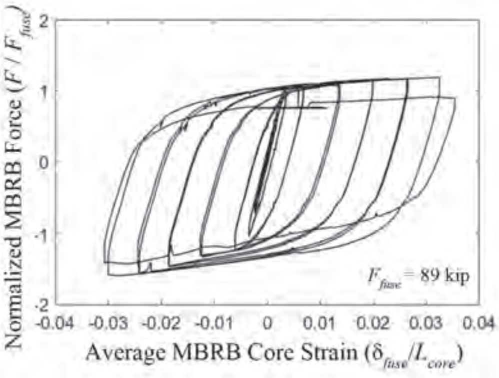

(c) MBRB behavior for SCB 3

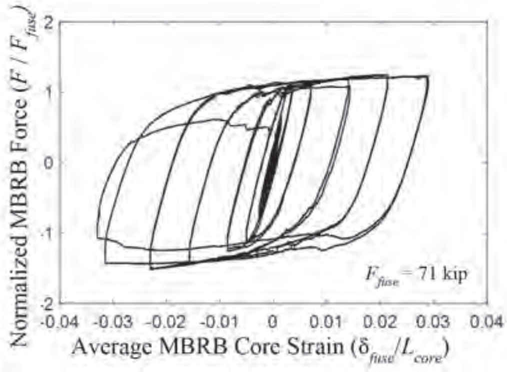

(d) MBRB behavior for SCB 4

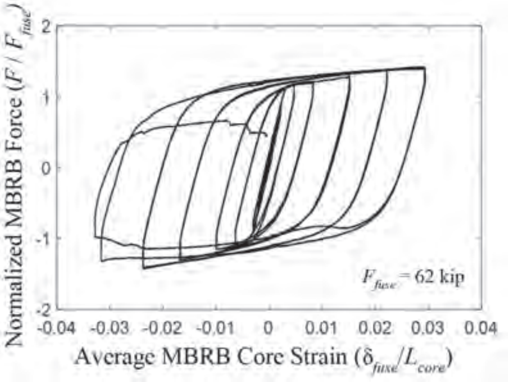

(e) MBRB behavior for SCB 5

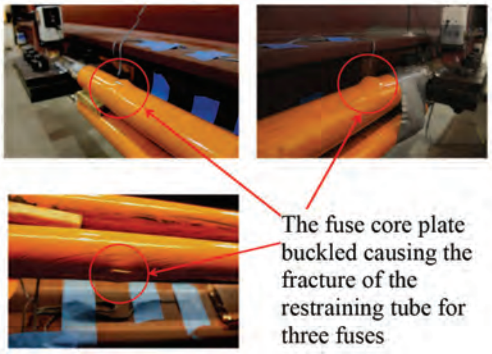
The fuse core plate buckled causing the fracture of the restraining tube for three fuses

(f) Pictures of final failure mode

Fig. 11. Response of miniature buckling restrained braces.

For the rest of the specimens (besides specimen SCB 2), the MBRBs were subjected to axial deformations up to approximately 3% average core strain before fracture of the MBRB core. The failure started with crushing of the gypsum cement that was used as grout, followed by protruding deformation in the restraining tube [see Figure 11(f)], at which time MBRB strength would degrade, and the core was assumed to fracture. The peak strains experienced by the MBRBs before fracture of the MBRB core ranged from 2.5% to 3.5% average core strain. These results are consistent with the component tests on the MBRBs (Maurya et al., 2016).

Fracture of one of the MBRB cores out of the four total MBRBs that were part of each specimen led to an approximate 25% drop in the MBRB strength as expected. For example, SCB 3 experienced a 25% drop in MBRB strength during the second cycle at 6% story drift, which was associated with 3% average core strain in the MBRB. One of the challenges associated with the current configuration of the SCB is that it uses four MBRBs such that the forces become unbalanced when one of the MBRB cores fracture. For this reason, and to protect the SCB body, the test was stopped after a significant enough drop in the MBRB force to suggest one of the MBRB cores fractured.

Figure 11 also shows that the strength in compression (negative core strain) was approximately 20% to 35% larger than the strength in tension (positive core strain). This trend is consistent with typical buckling restrained braces for which Poisson's effect causes the cross section of the core to expand during compression, which increases the friction between the core and the grout. This increased compression strength, as well as strain-hardening behavior of the MBRBs, was studied and characterized in Maurya et al. (2016).

SUMMARY AND CONCLUSIONS

A self-centering beam (SCB) moment frame is a seismic force-resisting system that can control residual drift during earthquakes and concentrate structural damage in replaceable elements. The body of the SCB consists of an I-shaped beam with a pair of concentric tubes at the bottom flange that are post-tensioned to encourage them to stay aligned, thus producing restoring force. Seismic energy is dissipated through miniature buckling restrained braces (MBRBs). SCB moment frames are expected to result in significantly smaller structural repair costs and shorter business downtime after large earthquakes as compared to conventional steel moment frames. In addition to this expected performance that is typical for all self-centering seismic systems, the SCB also offers two key advantages as compared to some existing self-centering systems: (1) The SCB can be shop fabricated and installed in the field with typical field construction methods (e.g., bolting). (2) The gap-opening mechanism that is typical to most self-centering systems is configured to be internal to the SCB; therefore, there is no deformation incompatibility with the floor diaphragm.

In this study, equations were derived to predict the flexural strength, self-centering capability, and deformation capacity of the SCB, and a design procedure was described. An experimental program was conducted including five specimens that were two-thirds scale relative to a prototype building and represented beams in both an upper and lower story. SCB specimens were tested in a setup consisting of a full, one-bay frame, and the set of specimens were designed to vary key design parameters such as the depth of the SCB, d_{SCB}, the self-centering ratio, α_{SC}, the initial PT stress ratio, α_{PTi}, the area of the post tensioning, A_{PT}, and the strength of the MBRB, F_{fuse}. Based on the results of the experimental program, the following seven observations were made:

1. It was found that the self-centering ratio was effective in controlling the ability of the SCB system to eliminate residual drift. Higher self-centering ratios, such as specimen SCB 3 with $\alpha_{SC} = 1.82$, were shown to retain their full self-centering ability (i.e., negligible drift when the lateral load is slowly removed from the peak drift) throughout the test. Phenomena like PT seating losses, PT strand yielding, PT wire fracture, and MBRB strain hardening cause a loss of self-centering capability during large cycles. However, past research shows that smaller self-centering ratios, as small as $\alpha_{SC} = 0.50$, can reliably eliminate residual drifts during design earthquakes because of a probabilistic self-centering in the presence of any restoring force.

2. The initial stiffness of the SCB was smaller than would be expected if the gap-opening mechanism were rigidly held closed. The reduced initial stiffness occurs because the bearing surfaces at the gap-opening interfaces are not perfectly flat or even, and there is a difference in axial stiffness of the tubes, which means the PT force is not shared evenly. While methods have been proposed to predict the initial stiffness of the SCB, it is expected that the initial stiffness could be increased by making the tubes the same area and using tighter tolerances for the bearing surfaces.

3. It was shown that the flexural strength at the two ends of the SCB are not independent, and thus, the total flexural strength (sum of the two ends) should be used in design. The measured SCB end moments were found to be similar until gap opening and then diverged such that the moment at one end was as much as 60% larger than the other end.

4. An equation was proposed to calculate flexural strength of the SCB and was shown to predict experimental

flexural strength within 5% on average. Equations to predict flexural strength associated with the MBRB and PT components were also proposed and shown to be reasonably accurate.

5. The SCB was shown to exhibit substantial deformation capacity and survived cycles of 6% story drift. Furthermore, the drift capacity can be controlled in design by careful selection of the initial post-tensioning stress, α_{PTi}, post-tensioning length, L_{PT}, and length of the MBRB core, L_{core}.
6. The restoring force mechanism and associated post-tensioning strands were shown to have predictable behavior. The equation to predict the story drift at PT yield was found to be slightly conservative, but it is still useful for design purposes. PT strands were subjected to cycles up to 1.2% average strain, and specimen SCB 2 was the only specimen that suffered two individual wire fractures, although this was linked to reseating of the PT strand anchorage during the post-tensioning process. The PT strands were shown to have considerable redundancy because each strand is composed of seven wires, and the wires fracture one at a time.
7. The MBRBs were shown to have full and stable hysteretic behavior up to approximately 3% axial strain over the core length before fracture. Fracture of one of the four MBRB cores led to an approximate 25% reduction in the MBRB strength as expected.

Based on this work, it is concluded that the SCB moment frame is a viable self-centering, seismic-force-resisting system that could be used in practice. Future research is warranted to improve the initial stiffness, and streamline the configuration and detailing to make the SCB more economically viable.

ACKNOWLEDGMENTS

This material is based upon the work supported by the National Science Foundation under grant CMMI-1200237. Any opinions, findings, conclusions, or recommendations expressed in this material are those of the authors and do not necessarily reflect the views of the National Science Foundation or other sponsors. In-kind donations for the large-scale tests were provided by Banker Steel, Hayes Industries, Weinstock Bros, and American Spring Wire.

REFERENCES

ACI (2003), *Special Hybrid Moment Frames Composed of Discretely Jointed Precast and Post-Tensioned Concrete Members*, ACI T1.2-03, reported by ACI Innovation Task Group 1 and Collaborators.

AISC (2016), *Seismic Provisions for Structural Steel Buildings*, ANSI/AISC 341-16, American Institute of Steel Construction, Chicago, Ill.

ASTM (2005), *Standard Specification for Steel Strand, Uncoated Seven Wire for Prestressed Concrete,* ASTM A416-05/A416M-05, ASTM International, West Conshohocken, Pa.

Bruce, T.L. (2014), “Behavior of Post-Tensioning Strand Systems Subjected to Inelastic Cyclic Loading,” M.S. Thesis, Virginia Tech, Blacksburg, Va.

Buchanan, A.H., Bull, D., Dhakal, R., MacRae, G., Palermo, A., and Pampanin, S. (2011), “Base Isolation and Damage-Resistant Technologies for Improved Seismic Performance of Buildings,” Technical Report 2011-02, Royal Commission of Inquiry into Building Failure Caused by the Canterbury Earthquakes, University of Canterbury, Christchurch, New Zealand.

Bruce, T.L. and Eatherton, M.R. (2016), “Behavior of Post-Tensioning Strand Systems Subjected to Inelastic Cyclic Loading,” *Journal of Structural Engineering*, Vol. 142, No. 10.

Chou, C.-C. and Chen, J.-H. (2011a), “Seismic Design and Shake Table Tests of a Steel Post-Tensioned Self-Centering Moment Frame with a Slab Accommodating Frame Expansion,” *Earthquake Engineering and Structural Dynamics*, Vol. 40, No. 11.

Chou, C.-C. and Chen, J.-H. (2011b), “Development of Floor Slab for Steel Post-Tensioned Self-Centering Moment Frames,” *Journal of Constructional Steel Research*, Vol. 67, pp. 1,621–1,635.

Chou, C.-C., Chen, J.-H., Chen, Y.-C., and Tsai, K.-C. (2006), “Evaluating Performance of Post-Tensioned Steel Connections with Strands and Reduced Flange Plates,” *Earthquake Engineering and Structural Dynamics*, Vol. 35, pp. 1,167–1,185.

Chou, C.-C. and Lai, Y.-J. (2009), “Post-Tensioned Self-Centering Moment Connections with Beam Bottom Flange Energy Dissipators,” *Journal of Constructional Steel Research*, Vol. 65, pp. 1,931–1,941.

Chou, C.-C., Wang, Y.-C., and Chen, J.-H. (2008), “Seismic Design and Behavior of Post-Tensioned Steel Connections Including Effects of a Composite Slab,” *Engineering Structures*, Vol. 30, pp. 3,014–3,023.

Christopoulos C., Filiatrault A., Uang C.-M., and Folz B. (2002), “Post-Tensioned Energy Dissipating Connections for Moment-Resisting Steel Frames,” *Journal of Structural Engineering*, Vol. 128, No. 9, pp. 1,111–1,120.

Darling, S.C., Eatherton, M.R., and Maurya, A. (2013), “Self-Centering Beams for Seismically Resilient Moment Frames,” *Proceedings of the 2013 SEI Structures Congress*, ASCE, Pittsburgh, Pa.

Dowden, D.M. and Bruneau, M. (2011), "NewZ-BREAKSS: Post-Tensioned Rocking Connection Detail Free of Beam Growth," *Engineering Journal*, AISC, Vol. 42, No. 2, pp. 153–158.

Eatherton, M. and Hajjar, J.F. (2011), "Residual Drifts of Self-Centering Systems Including Effects of Ambient Building Resistance," *Earthquake Spectra*, Vol. 27, No. 3.

Eatherton, M.R., Fahnestock, L.A., and Miller, D. (2014), "Computational Study on the Behavior of Self-Centering Buckling Restrained Braces," *Earthquake Engineering and Structural Dynamics*, Vol. 43, No. 13, pp. 1,897–1,914.

Eatherton, M.R., Ma, X., Krawinkler, H., Mar, D., Billington, S., Hajjar, J.F., and Deierlein, G.G. (2014), "Design Concepts for Controlled Rocking of Self-Centering Steel Braced Frames," *Journal of Structural Engineering*, Vol. 140, No. 11.

Eatherton, M.R. and Maurya, A. (2018), "Computational Evaluation of Self-Centering Beam Moment Frame (SCB-MF) in Multistory Buildings," *Eleventh U.S. National Conference on Earthquake Engineering*, June 25–29, Los Angeles, Calif.

El-Sheikh, M.T.M. (1997), "Seismic Analysis, Behavior, and Design of Unbonded Post-Tensioned Precast Concrete Frames," Ph.D. Dissertation, Lehigh University, Bethlehem, Pa.

Englekirk, R.E. (2002), "Design-Construction of the Paramount—A 39-Story Precast Prestressed Concrete Apartment Building," *PCI Journal*, July–August, pp. 56–71.

Fang, C., Wang, W., Ricles, J., Yang, X., Zhong, Q., Sause, R., and Chen, Y. (2018), "Application of an Innovative SMA Ring Spring System for Self-Centering Steel Frames Subject to Seismic Conditions," *Journal of Structural Engineering*, Vol. 144, No. 8.

Farmani, M.A. and Ghassemieh, M. (2016), "Shape Memory Alloy-Based Moment Connections with Superior Self-Centering Properties," *Smart Materials and Structures*, Vol. 25, pp. 1–17.

Garlock, M.E.M. and Li, J. (2008), "Steel Self-Centering Moment Frames with Collector Beam Floor Diaphragms," *Journal of Constructional Steel Research*, Vol. 64, pp. 526–538.

Garlock, M.M., Sause, R., and Ricles, J.M. (2007), "Behavior and Design of Post-Tensioned Steel Frame Systems," *Journal of Structural Engineering,* Vol. 133, pp. 389–399.

Gupta, A. and Krawinkler, H. (1999), "Seismic Demands for Performance Evaluation of Steel Moment Resisting Frame Structures," John A. Blume Earthquake Engineering Center Report Number 132.

Hawkins, N.M. and Ghosh, S.K. (2004), "Requirements for the Use of PRESSS Moment-Resisting Frame Systems," *PCI Journal*, March–April, pp. 98–103.

Huang, X., Zhou, Z., Eatherton, M.R., Zhu, D., and Guo, C. (2019), "Experimental Investigation of Self-Centering Beams for Moment-Resisting Frames," *Journal of Structural Engineering*, Vol. 146, No. 3.

Huang, X., Zhou, Z., Xie, Q., Xue, R., and Zhu, D. (2017), "Force Distribution Analysis of Self-Centering Coupled-Beams for Moment-Resisting-Frames without Floor Elongation," *Engineering Structures*, Vol. 147, pp. 328–344.

Kim, H.-J. and Christopoulos, C. (2008), "Friction Damped Posttensioned Self-Centering Steel Moment Resisting Frames," *Journal of Structural Engineering*, Vol. 134, No. 11, pp. 1,768–1,779.

Kim, H.-H. and Christopoulos, C. (2009), "Seismic Design Procedure and Seismic Response of Post-Tensioned Self-Centering Steel Frames," *Earthquake Engineering and Structural Dynamics*, Vol. 38, pp. 355–376.

Kurama, Y. C., Weldon, B.D., and Shen, Q. (2006), "Experimental Evaluation of Post-Tensioned Hybrid Coupled Wall Subassemblages," *Journal of Structural Engineering*, Vol. 132, No. 7.

Lin, Y.-C. (2015), "Steel Sliding-Controlled Coupled Beam Modules: Development and Seismic Behavior for a Moment Resisting Frame," *Engineering Structures*, Vol. 99, pp. 726–736.

Lin, Y.-C., Sause, R., and Ricles, J.M. (2013), "Seismic Performance of a Large-Scale Steel Self-Centering Moment-Resisting Frame: MCE Hybrid Simulations and Quasi-Static Pushover Tests," *Journal of Structural Engineering*, Vol. 139, No. 7, pp. 1,227–1,236.

MacRae, G.A. and Gunasekaran, U. (2006), "A Concept for Consideration of Slab Effects on Building Seismic Performance," *Proceedings of the New Zealand Society for Earthquake Engineering Conference*, March 10–12, Napier, New Zealand.

Maurya, A. (2016), "Experimental and Computational Investigation of a Self-Centering Beam Moment Frame (SCB-MF)," Ph.D. Dissertation, Virginia Tech, Blacksburg, Va.

Maurya, A. and Eatherton, M.R. (2016), "Experimental Study of the Restoring Force Mechanism in the Self-Centering Beam (SCB)," *Frontiers of Structural and Civil Engineering*, Vol. 10, No. 3, pp. 272–282.

Maurya, A., Eatherton, M.R., Matsui, R., and Florig, S.H. (2016), "Experimental Investigation of Miniature Buckling Restrained Braces for Use as Structural Fuses," *Journal of Constructional Steel Research*, Vol. 127, pp. 54–65.

Miller, D.J., Fahnestock, L.A., and Eatherton, M.R. (2012), "Development and Experimental Validation of a Nickel-Titanium Shape Memory Alloy Self-Centering Buckling-Restrained Brace," *Engineering Structures*, Vol. 40, pp. 288–298.

Priestley, M.J.N. (1991), "Overview of PRESSS Research Program," *PCI Journal*, July–August, pp. 50–57.

Priestley, M.J.N., Sritharan, S., Conley, J.R., and Pampanin, S. (1999), "Preliminary Results and Conclusions from the PRESS Five-Story Precast Concrete Test Building," *PCI Journal*, Vol. 44, No. 6, pp 42–67.

Ricles, J., Sause, R., Garlock, M., and Zhao, C. (2001), "PostTensioned Seismic-Resistant Connections for Steel Frames," *Journal of Structural Engineering*, Vol. 127, No. 2, pp. 113–121.

Stone, W.C., Cheok, G.S., and Stanton, J.F. (1995), "Performance of Hybrid Moment-Resisting Precast Beam-Column Concrete Connections Subjected to Cyclic Loading," *ACI Structural Journal*, March–April, pp. 229–249.

Vasdravellis, G., Karavasilis, T.L., and Uy, B. (2013), "Finite Element Models and Cyclic Behavior of Self-Centering Post-Tensioned Connections with Web Hourglass Pins," *Engineering Structures*, Vol. 52, pp. 1–16.

Wang, W., Du, X., Zhang, Y., and Chen, Y. (2017), "Experimental Investigation of Beam-Through Steel Frames with Self-Centering Modular Panels," *Journal of Structural Engineering*, Vol. 143, No. 5.

Wolski, M., Ricles, J.M., and Sause, R. (2006), "Seismic Resistant Self-Centering Steel Moment Resisting Frames with Bottom Flange Friction Devices," *Proceedings of the Fifth International Conference on Behaviour of Steel Structures in Seismic Areas STESSA*, August 14–17, Yokohama, Japan.

Technical Note

Unbraced Length Requirements for Steel Special Cantilever Column Systems

ROBERT J. WALTER and CHIA-MING UANG

ABSTRACT

AISC *Seismic Provisions* Section E6.4b for steel special cantilever column systems (SCCS) requires clarification based on inquiries to the AISC Steel Solutions Center. In the 2016 edition, it is unclear if bracing is required for all special cantilever columns or for columns with unbraced lengths that exceed the maximum beam brace spacing of L_b per Section D1.2a for moderately ductile members. Instead of using Equation D1-2, which is applicable to I-shaped beams only, equations for SCCS columns have been derived for both I-shaped members and rectangular HSS or box-shaped members. The proposed revision provides specific situations when bracing is required.

Keywords: AISC *Seismic Provisions*, steel special cantilever column system, bracing.

INTRODUCTION

ASCE/SEI 7, *Minimum Design Loads and Associated Criteria for Buildings and Other Structures*, hereafter referred to as ASCE/SEI 7 (ASCE, 2016), specifies two steel cantilevered column systems: special cantilever column systems (SCCS) and ordinary cantilever column systems (OCCS), where the values of the response modification factor, *R*, are 2½ and 1¼, respectively. Although these systems have an *R* factor less than 3 due to a lack of system redundancy, they are required to satisfy the requirements in the AISC *Seismic Provisions for Structural Steel Buildings*, hereafter referred to as the AISC *Seismic Provisions* (AISC, 2016a). OCCS are intended to provide a minimal level of inelastic rotation capability at the base of the column. This system is permitted in Seismic Design Categories B and C and to heights not exceeding 35 ft. OCCS are also permitted in Seismic Design Categories D, E, and F with a height limit of up to 65 ft when meeting the requirements of ASCE 7, Section 12.2.5.6. A low *R* value of 1¼ is assigned due to the system's limited inelastic capacity and lack of redundancy. OCCS have two requirements beyond those in the AISC *Specification for Structural Steel Buildings*, hereafter referred to as the AISC *Specification* (AISC, 2016b). First, columns shall be designed using the load combinations, including the overstrength seismic load. Second, the required axial strength, P_{rc}, shall not exceed 15% of the available axial strength, P_c, for the load combinations, including the overstrength seismic load.

SCCS are intended to provide a limited level of inelastic rotation capability at the base of the column. This system is permitted in Seismic Design Categories B through F but is limited to heights not exceeding 35 ft. The required axial strength has the same limitation as OCCS to help reduce the likelihood of collapse. The column members are required to satisfy the width-to-thickness ratios for highly ductile members. However, the lateral bracing requirement for moderately ductile members is required due to the relatively low inelastic demand expected and the practical difficulty in achieving bracing in many of these structures. The purpose of the bracing is to restrain lateral-torsional buckling (LTB) of the column.

According to AISC *Seismic Provisions* Section D1.2b, the maximum beam brace spacing for highly ductile members is

$$L_b = 0.095 r_y E \big/ \left(R_y F_y\right) \tag{1}$$

and according to Section D1.2a, the maximum beam brace spacing for moderately ductile members is

$$L_b = 0.19 r_y E \big/ \left(R_y F_y\right) \tag{2}$$

Although not specifically stated in AISC *Seismic Provisions* Section D1.2, these two requirements are intended for doubly symmetric I-shape beams. For the next edition of the AISC *Seismic Provisions*, new maximum brace spacing for SCCS with I-shaped columns as well as rectangular HSS or box-shaped columns are proposed.

Robert J. Walter, Principal Structural Engineer, McDermott, Plainfield, Ill. Email: Robert.walter@mcdermott.com (corresponding).

Chia-Ming Uang, Professor, Department of Structural Engineering, University of California, San Diego, La Jolla, Calif. Email: cmu@ucsd.edu.

Paper No. 2019-20

BASIS OF CURRENT SEISMIC BEAM BRACING REQUIREMENTS

A review of the historical development of Equation 1 for beam design is first presented. The maximum spacing limits for lateral bracing of beams in the earlier editions of the AISC *Seismic Provisions* are based on the lateral bracing requirement for I-shaped sections using plastic design from AISC LRFD *Specification* Section F1.1 (AISC, 1986):

$$L_{pd} = \frac{3{,}600 + 2{,}200\left(M_1/M_p\right)}{F_y} r_y \qquad (3)$$

where M_1 is the smaller moment at the end of the unbraced length, M_p is the plastic moment (replaced by M_2 in later editions), and M_1/M_p is positive when moments cause reverse curvature. Note that Equation 3 is based on tests of continuous beams for a target rotation capacity of 3, where the rotation capacity is defined as the ratio between plastic rotation and yield rotation (Bansal, 1971; Yura et al., 1978). Introducing the modulus of elasticity, E, to normalize F_y, Equation 3 is converted to the following form, which is AISC *Specification* Equation A-1-5 (AISC, 2016b):

$$L_{pd} = \left(0.12 - 0.076\frac{M_1'}{M_2}\right)\frac{E}{F_y} r_y \qquad (4)$$

where M_1' is the effective moment at the end of the unbraced length opposite from M_2, M_2 is the larger moment at the end of the unbraced length, $M_1' = M_1$ when the midspan moment is not larger than the average of M_1 and M_2, and $M_1' = M_2$ is negative when moments cause reverse curvature. Assuming that (1) the effect of the gravity load component is small and can be ignored and (2) the inflection point due to the seismic effect is at the midspan of a moment frame beam, M_1/M_2 equals +1.0 per Equation 3 [see Figure 1(a)]. However, for seismic applications, the AISC *Seismic Provisions* implicitly assume a conservative seismic moment diagram like that shown in Figure 1(b) with M_1/M_2 equal to −½. Substituting this latter moment ratio and introducing the modulus of elasticity, E, into Equation 3 gives the following:

$$L_b = \frac{2500 r_y}{F_y} = 0.086\frac{r_y E}{F_y} \qquad (5)$$

To include the R_y factor in Equation 5 with an assumed value of 1.1, Equation 5 becomes Equation 1 for highly ductile beams since the 2016 edition of the AISC *Seismic Provisions*, which is required for beam design in special moment frames (SMF).

The requirement for the maximum beam brace spacing of I-shaped beams in systems like intermediate moment frames (IMF) is more relaxed than that in SMF because, according to the Commentary of the 2005 AISC *Seismic Provisions* (AISC, 2005), a lower story-drift angle (0.02 rad) is required in comparison to that required for SMF (0.04 rad). The AISC *Seismic Provisions* assume that the maximum beam brace spacing for IMF is twice that for SMF (i.e., Equation 2).

PROPOSED L_b FOR SCCS COLUMNS

The AISC *Seismic Provisions* specify a maximum brace spacing for SCCS (Equation 2), which was developed for I-shaped beams in IMF with an assumed moment gradient. Instead of using Equation 2 for columns in SCCS, the maximum brace spacing can be derived directly from the original formula (Equation 3) by using the actual moment gradient. The moment, M_1, at the top end of the column can be equal to zero. However, it can also be nonzero and can be determined easily in the design process—for example, an SCCS used as an inverted pendulum-type structure. Therefore, to accommodate the possible loading scenarios of cantilever columns, the moment ratio term is retained from the original equations. Note that F_y in the original development of Equation 3 represents the actual, not nominal, yield stress. Referring to Equation 4, which is equivalent to Equation 3 but with an opposite definition of the sign convention for the moment gradient (see Figure 1), the F_y term can be substituted for R_yF_y directly for implementation in the AISC *Seismic Provisions*:

$$L_b = \left(0.12 - 0.076\frac{M_1}{M_2}\right)\frac{r_y E}{R_y F_y} \qquad (6)$$

where M_1/M_2 is positive when moments cause single curvature.

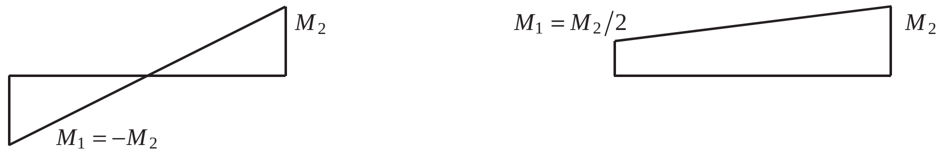

(a) $M_1/M_2 = +1$ *(Eq. 3) or* $= -1$ *(Eq. 4)*

(b) $M_1/M_2 = -½$ *(Eq. 3) or* $= +½$ *(Eq. 4)*

Fig. 1. Assumed seismic moment diagrams.

Equation 6 is applicable for SCCS I-shaped columns bent about their major axis. The AISC *Seismic Provisions* do not provide the maximum brace spacing for rectangular HSS or box-shaped members bent about their major axis. To derive L_b for this case, start with AISC *Specification* Equation A-1-7:

$$L_{pd} = \left(0.17 - 0.10\frac{M_1'}{M_2}\right)\frac{E}{F_y}r_y \geq 0.10\frac{E}{F_y}r_y \tag{7}$$

Replacing M_1' with M_1 and F_y with R_yF_y, Equation 7, for rectangular HSS or box-shaped members bent about their major axis, becomes:

$$L_b = \left(0.17 - 0.10\frac{M_1}{M_2}\right)\frac{r_yE}{R_yF_y} \geq 0.10\frac{r_yE}{R_yF_y} \tag{8}$$

APPLICATION OF CANTILEVER COLUMN BRACING

OCCS do not require bracing. SCCS require bracing to restrain LTB so that flexural yielding at the column base can be developed. The bracing is not intended to provide column stability or prevent sidesway. The LTB limit state does not apply to round HSS, square HSS, square box sections, or any cross section bent about its minor axis. Thus, exceptions are proposed for the next edition of the AISC *Seismic Provisions* to state that bracing is not required for these types of members. An additional exception is proposed to allow the usage of short columns without bracing by conservatively limiting the column length to half the maximum bracing spacing.

Point torsional bracing is likely to be the best choice for LTB bracing because lateral bracing may cause the seismic force-resisting system to behave as something other than a cantilever column system. Point torsional bracing must meet the flexural strength and stiffness requirements for beam torsional bracing in AISC *Specification* Appendix 6. As an example, point torsional bracing can be achieved by attaching beam(s) to the column, preventing torsional rotation of the column. Cantilever column systems can act as a cantilever column in one direction and can be used with other systems (moment or braced frames) in the orthogonal direction. The seismic force-resisting systems in the orthogonal direction can be used to provide the required lateral or point torsional bracing for the cantilever column system.

CONCLUSION

The proposed equations for the maximum brace spacing of SCCS are an improvement over current requirements because an appropriate moment ratio can be used. The proposed equations for major-axis bending are also specific to member cross-section types. Equation 6 is for I-sections, and Equation 8 is for rectangular HSS or box-shaped members. Clarity on the purpose of the bracing, conditions when the bracing is and is not required, and guidance on the type of bracing are provided.

REFERENCES

AISC (1986), *Load and Resistance Factor Design Specification for Structural Steel Buildings*, American Institute of Steel Construction, Chicago, Ill.

AISC (2005), *Seismic Provisions for Structural Steel Buildings*, ANSI/AISC 341-05, American Institute of Steel Construction, Chicago Ill.

AISC (2016a), *Seismic Provisions for Structural Steel Buildings*, ANSI/AISC 341-16, American Institute of Steel Construction, Chicago Ill.

AISC (2016b), *Specification for Structural Steel Buildings*, ANSI/AISC 360-16, American Institute of Steel Construction, Chicago, Ill.

ASCE (2016), *Minimum Design Loads and Associated Criteria for Buildings and Other Structures*, ASCE/SEI 7-16, American Society of Civil Engineers, Reston, Va.

Bansal, J.P. (1971), "The Lateral Instability of Continuous Steel Beams," Ph.D. Thesis, University of Texas, Austin, Texas.

Yura, J.A., Galambos, T.V., and Ravindra, K. (1978), "The Bending Resistance of Steel Beams," *Journal of the Structural Division*, ASCE, Vol. 104, No. ST9, pp. 1,355–1,370.

Steel Structures Research Update

Continuity Plate Design for Special and Intermediate Moment Frames

JUDY LIU

INTRODUCTION

Recent advances in continuity plate design for special and intermediate moment frames are highlighted. The featured research includes a comprehensive experimental and computational study by Dr. Chia-Ming Uang and Dr. Mathew Reynolds. Chia-Ming Uang is a professor of structural engineering at the University of California, San Diego (UCSD). Dr. Uang is an internationally recognized leader in structural steel research and standards development, with an emphasis in seismic-resistant design. Dr. Uang's numerous accolades include AISC's Special Achievement Award in 2007, the T.R. Higgins Lectureship Award in 2015, and this year, AISC's Lifetime Achievement Award. Dr. Reynolds completed this research as his doctoral work at UCSD under Dr. Uang's guidance and is now working as a bridge engineer for Kiewit in Burnaby, British Columbia, Canada.

The full-scale test program and computational parametric study supported the use of fillet welds to replace expensive complete-joint-penetration (CJP) groove welds adjoining the continuity plate to column flanges. A simplified weld design procedure, as well as local buckling design criteria, are being developed for potential inclusion in the next edition of the AISC *Seismic Provisions for Structural Steel Buildings* (AISC, 2016a). The motivation for the study, the proposed design methodology, and selected experimental and computational results are presented.

BACKGROUND AND MOTIVATION

There are some possibly conservative design and detailing requirements for prequalified connections in special and intermediate moment frames. The conservative provisions include welding and geometric requirements for continuity plates and come with cost implications. Continuity plates, shown in Figure 1, stiffen the column for the concentrated forces and deformations from the beam flanges.

Continuity plates are required when the column has insufficient strength for the concentrated forces or does not satisfy prescriptive geometric limits. Applicable limit states include local flange bending (LFB), web local yielding (WLY), and web local crippling (WLC) of the column. The available strength of the column is calculated following the AISC *Specification* (AISC, 2016b). AISC *Seismic Provisions* Equation E3-8 also requires continuity plates when the column flange thickness is less than the beam flange width divided by 6 (AISC, 2016a). In this study, the minimum unstiffened column flange thickness requirement has been named the "Lehigh criterion," acknowledging the source.

The continuity plates and their welds have additional, sometimes expensive, requirements. The continuity plate must be at least 50% as thick as the adjacent beam flange thickness for exterior (one-sided) connections. For interior (two-sided) connections, the continuity plate thickness must be at least 75% that of the thicker adjacent beam flange. The weld between the continuity plate and the column flange is required to be a CJP groove weld. Compared to fillet welds, the CJP groove welds are more expensive due to the fabrication of the beveled plates, fabrication and installation of backing bars, potential for additional weld volume, and more stringent inspection requirements. From the fabrication point of view, it would be highly desirable if fillet welds were permitted.

Additional motivation for this investigation came from a pilot study by Mashayekh and Uang (2018). The pilot study included tests of two exterior reduced beam section (RBS) connections with fillet-welded continuity plates. The study was focused on use of an elastic, flexibility design method for the continuity plates originally developed by Tran et al. (2013). But continuity plates of one specimen were intentionally undersized to permit yielding. The satisfactory performance observed for the connection with continuity plate yielding inspired, in part, the test program for the featured study.

RESEARCH OBJECTIVES AND PROPOSED DESIGN METHODOLOGY

The overarching research goal was to develop and validate a more efficient, plastic design methodology for continuity plates and use rationally designed fillet welds to attach continuity and doubler plates. The focus for this article is on

---

Judy Liu, PhD, Research Editor of the AISC *Engineering Journal*, Professor, Oregon State University, School of Civil and Construction Engineering, Corvallis, Ore. Email: judy.liu@oregonstate.edu

the continuity plates and their welds. For the objective of improving the economy of continuity plates, the proposed methods for sizing the plate and fillet welds were verified experimentally and numerically. Requirements dictating the use of continuity plates—for example, the Lehigh criterion—were also studied. Full-scale testing provided supporting evidence in two phases: the first phase investigated reduced beam section (RBS) one-sided connections, and the second phase examined welded unreinforced flange–welded web (WUF-W) two-sided connections. Detailed finite element analysis was used to parametrically study and verify the proposed design methodology.

The proposed plastic methodology for the continuity plates has basis in the current provisions of the AISC *Specification* (AISC, 2016b). The demand on the continuity plate considers the beam flange force and the column strength associated with FLB, WLY, and WLC. The continuity plate is analyzed for in-plane axial and shear forces, and its ultimate strength is verified with a plastic interaction equation (Dowswell, 2015). A capacity design philosophy was used to develop a simple rule for sizing the fillet welds that join the continuity plates and the column flanges. The strength of a transverse, double-sided fillet weld of size w was compared to the nominal yield strength of the plate. For an A572 Gr. 50 continuity plate of thickness t_{cp} and a fillet weld made with a matched weld electrode, the rule is $w = (3/4)t_{cp}$.

EXPERIMENTAL TESTING

The test setup and loading were designed to impose deformations corresponding to increasing levels of interstory drift on moment frame subassemblies. Figure 2 shows an interior moment connection specimen in a horizontal test setup. The cruciform test subassembly represented a portion of a prototype moment frame, extending half the bay width to either side for each beam and half the story height above and below the beam-column joint. The ends of the test beams and columns were at assumed inflection points in the prototype moment frame. The loading corbels, hinge, and clevis supports in the test frame were designed to provide the appropriate boundary conditions. Lateral beam bracing was also provided in accordance with the AISC *Seismic Provisions* requirements for highly ductile members. For the interior moment connection tests, two 500-kip hydraulic actuators were used in displacement control for the cyclic loading protocol prescribed in the AISC *Seismic Provisions* (AISC, 2016a). The imposed displacements were applied equal and opposite on either side of the connection. The exterior moment connections were tested using a similar setup but in an upright position and with a single 220-kip hydraulic actuator. Additional test setup, loading, and instrumentation information can be found in Reynolds (2020).

Test Specimens

The test program included 10 full-scale specimens. These moment connection specimens were designed to evaluate the efficacy of economized continuity plate and doubler plate weld details (Reynolds, 2020). Six one-sided, or exterior, RBS connections (C series) were tested in phase 1. Four two-sided, or interior, WUF-W connections (W series) were tested in phase 2. The beams and columns were all ASTM A992 W-shape sections. Beam, column, and connection

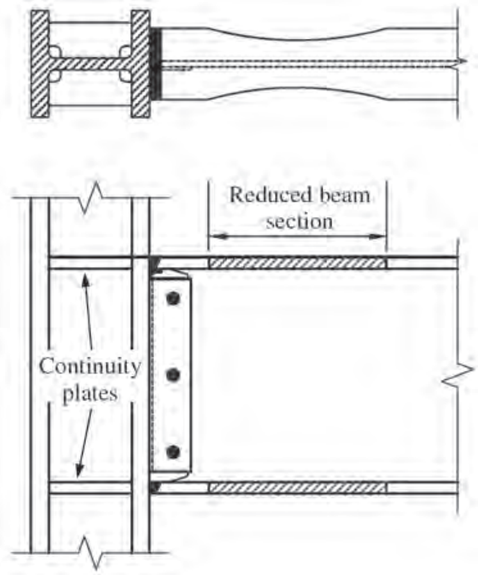

Fig. 1. Reduced beam section (RBS) moment connection with continuity plates.

design and detailing satisfied the AISC *Seismic Provisions* (AISC, 2016a) and the AISC *Prequalified Connections for Special and Intermediate Steel Moment Frames for Seismic Applications* (AISC, 2020) requirements except as noted. The continuity and doubler plates were fabricated from ASTM A572 Gr. 50 steel. Simulated field welding was used for the beam top and bottom flange CJP groove welds and beam web CJP groove weld. The continuity plate and doubler plate weld electrodes satisfied notch-toughness requirements for demand critical welds specified in AWS D1.8 (AWS, 2016).

The phase 1 RBS specimens were used to explore the proposed design methodology for the continuity plates and their welds. FLB and WLY were considered in the plastic design methodology. It was noted that WLC rarely governs in special moment frames (SMFs) using rolled wide-flange shapes. A number of specimens were used to test the current requirement that an unstiffened column flange is at least as thick as the adjacent beam flange width divided by 6 (AISC, 2016a), the Lehigh criterion.

The phase 2 WUF-W specimens were used to investigate the validity of the proposed methodology for continuity plates with higher demands associated with a two-sided WUF-W connection. High panel-zone shear demands dictated the use of doubler plates in all specimens; three of the four specimens used extended doubler plates that protrude beyond the continuity plate at the beam flange elevation. The final specimen used a doubler plate cut flush with the inside face of the continuity plates.

Three test specimens, two RBS and one WUF-W, will be described here. Specimens C5, C6, and W2 were all designed to investigate the validity of using the plastic distribution to estimate the required strength of the continuity plate. Some test specimen details are provided in the following sections. Additional details for these specimens and the rest of the test program can be found in Reynolds and Uang (2019).

Reduced Beam Section (RBS) Specimen C5

The panel zone, continuity plate thickness, and weld size were important parameters for specimen C5 [Figure 3(a)]. The reduced section in the W36×150 beam had dimensions as shown in Figure 3(b). The W14×211 column was designed to have a weak panel zone, with a demand-to-capacity ratio of 1.18. The intent was to exacerbate column kinking. The continuity plates were sized using the plastic design method, with a deliberately high width-to-thickness ratio of 16.0. The continuity plates did not satisfy the AISC *Seismic Provisions* requirement of a thickness at least half that of the beam flange thickness for exterior connections. Local buckling, together with column kinking, was expected to impose significant inelastic demands on the continuity plates and the welds. Meanwhile, the continuity plate welds to the column flanges were sized using the proposed $w = (3/4)t_{cp}$ rule.

Reduced Beam Section (RBS) Specimen C6

Continuity plate thickness was also an important parameter for specimen C6. The reduced section in the W30×116 beam had dimensions as shown in Figure 4. The continuity plates were sized using the plastic design method. The plates did satisfy the AISC *Seismic Provisions* requirement of a thickness at least half that of the beam flange thickness for exterior connections. Meanwhile, the continuity plate welds to the W24×176 column flanges were conservatively sized as $w = t_{cp}$. The intent of the oversized fillet welds was to avoid possible premature failure and to allow for investigation into the effects of galvanization with a companion specimen C6-G.

Fig. 2. Interior moment connection test setup.

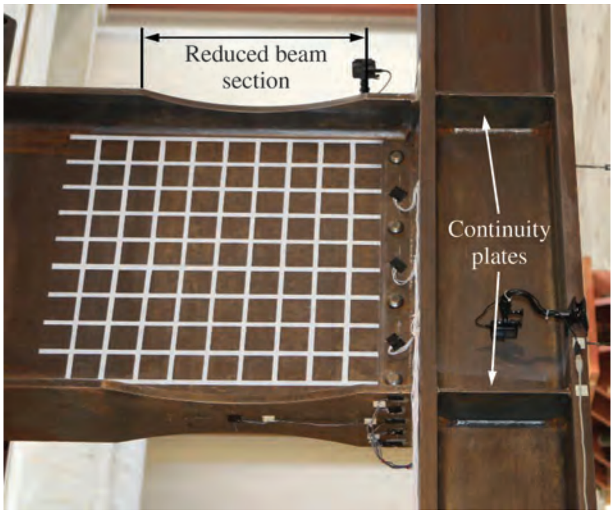

(a) Specimen C5 before testing

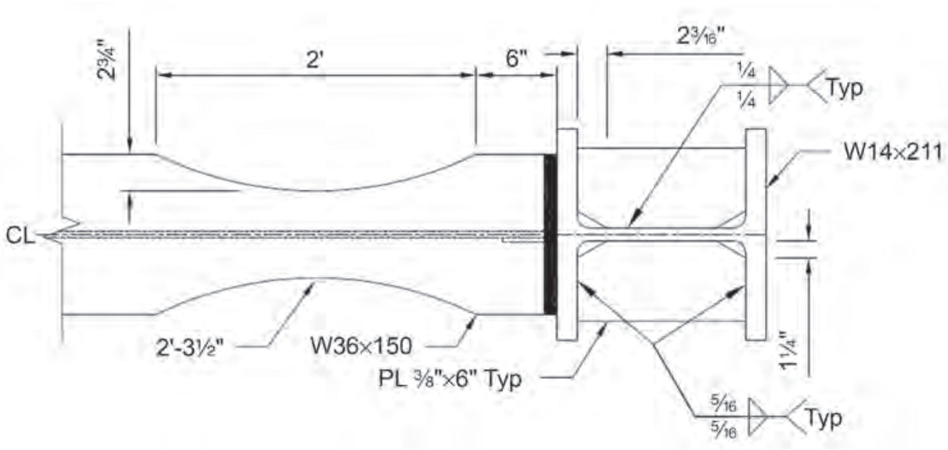

(b) RBS and continuity plate weld details

Fig. 3. One-sided RBS connections.

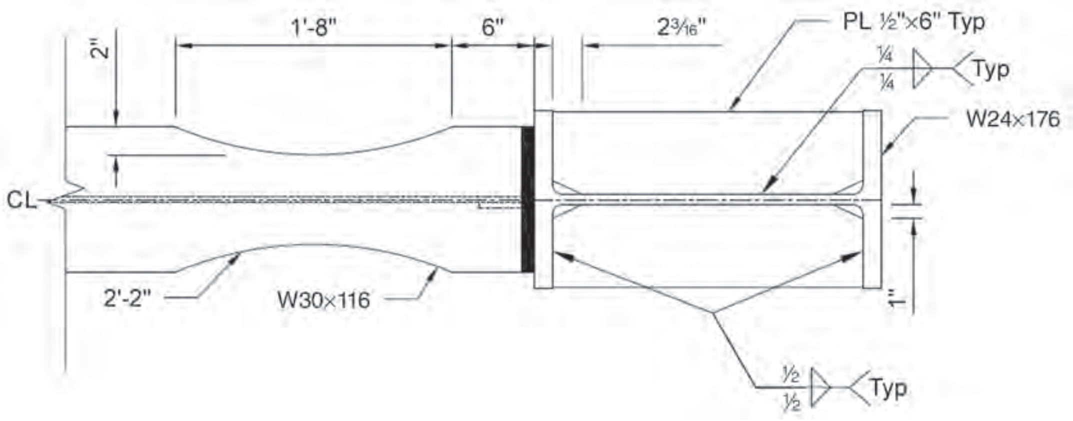

Fig. 4. Section through specimen C6 column showing continuity plates and RBS flange cuts.

Welded Unreinforced Flange–Welded Web (WUF-W) Specimen W2

Specimen W2 used a W33×141 beam and featured continuity and doubler plates, as shown in Figures 5 and 6. The continuity plates were intentionally overloaded to investigate any detrimental effects. The continuity plates satisfied the AISC *Seismic Provisions* requirement of a thickness of at least three-quarters of the beam flange thickness for interior connections. According to the plastic methodology, the continuity plates were undersized, with a demand-to-capacity ratio of 1.43. The continuity plate welds to the W27×217 column flanges were sized using the proposed $w = (3/4)t_{cp}$ rule. A pair of ¾-in. doubler plates extended 6 in. above and below the beam flange elevations. Vertical partial-joint-penetration (PJP) groove welds connected the doubler plates to the columns.

Experimental Results

Specimens C5, C6, and W2 confirmed the proposed design methodology and exhibited satisfactory performance. The continuity plate-to-column flange welds showed no signs of distress for the 7 (of 10) specimens tested with a continuity plate in this research program. Despite specimen W2's intentionally undersized continuity plates, there was no continuity plate yielding and only minor panel-zone yielding in the doubler plates. The global load-displacement and moment-story drift response for specimen C5 are shown in Figure 7. Similar results were recorded for specimen C6. The column shear versus story drift response for specimen W2 is shown in Figure 8. All 10 specimens tested in this research satisfied the strength and story drift angle acceptance criteria of 0.04 rad (AISC, 2016a).

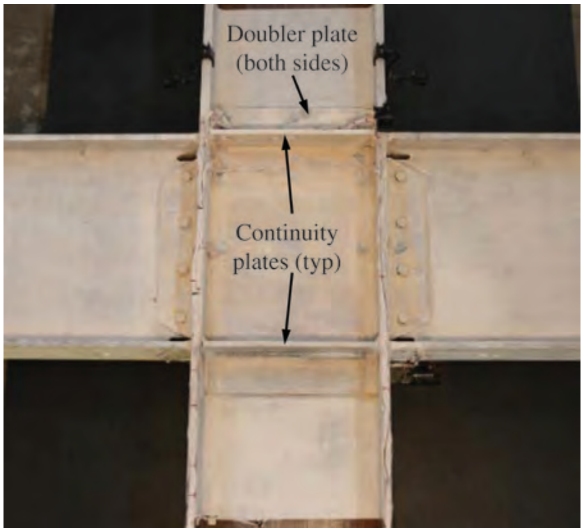

Fig. 5. Specimen W2 before testing.

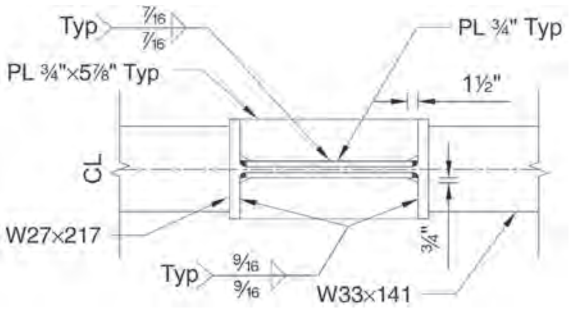

Fig. 6. Specimen W2 continuity and doubler plate details.

Specimen C5 exhibited ductile behavior and experienced significant inelastic demands from column kinking and local buckling in the beam web, beam flange, and continuity plate [Figure 9(a).] Beam web and flange local buckling within the reduced section were not observed until the 0.04-rad drift cycles. A bottom flange continuity plate also started to develop local buckling at 0.04-rad drift. By 0.05-rad drift, local buckling was observed in both flanges, as well as in a continuity plate on either side of the web at the top and bottom flanges. Column kinking was observed throughout the testing of the specimen. Ductile tearing of the beam top flange CJP groove weld was first observed in the second negative excursion of 0.03-rad drift. The specimen eventually failed by fracture of the beam top flange CJP groove weld after completing two cycles of 0.05-rad drift, as shown in Figure 9(b). Slight beam lateral-torsional buckling was also observed at the end of testing.

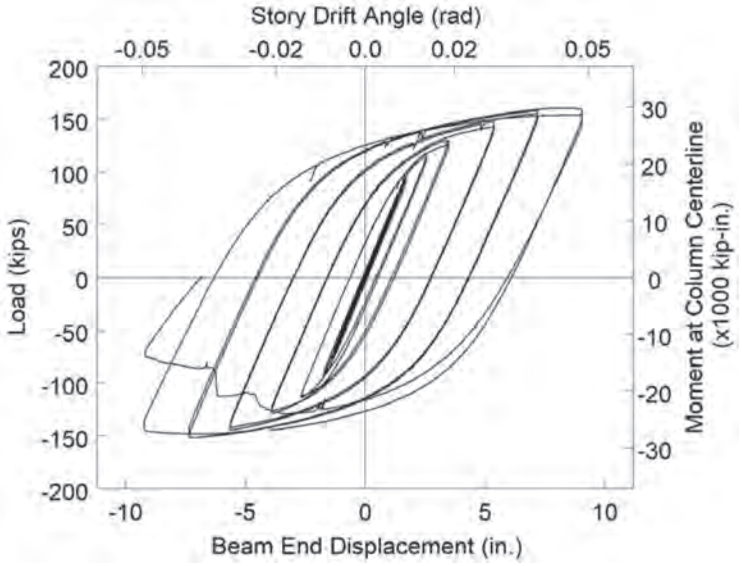

Fig. 7. Load-displacement and moment-story drift response for specimen C5.

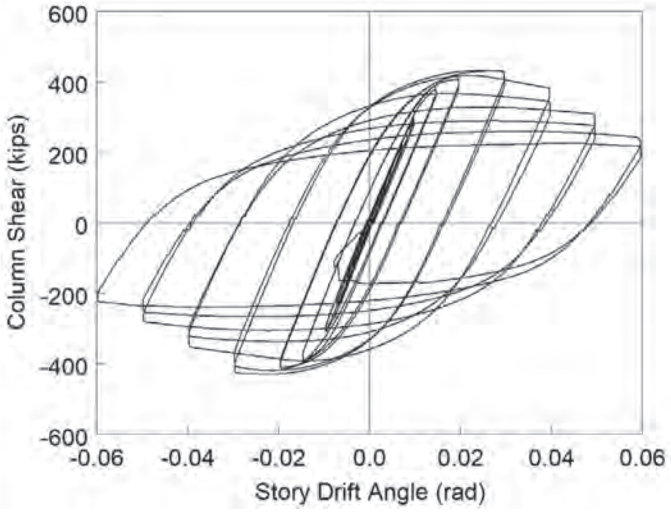

Fig. 8. Specimen W2 column shear versus story drift angle.

Specimen C6 also exhibited ductile behavior. Beam bottom flange yielding in the reduced section was observed during the 0.01-rad drift cycles. Panel-zone yielding commenced during the 0.015-rad cycles. Beam web buckling and beam flange local buckling as shown in Figure 10(a) did not start until the first cycle of 0.04-rad drift. Minor lateral-torsional buckling could also be observed. Minor ductile tearing of the beam top flange CJP groove weld began in the first negative excursion to 0.03-rad drift. In the 0.05-rad cycles, specimen C6 experienced a sudden fracture propagation at –0.037 rad, as shown in Figure 10(b), which led to complete fracture at –0.05-rad drift.

It should be noted that only a few RBS specimens failed at the beam flange-to-column CJP groove weld. Furthermore, ductile tearing preceded the eventual weld fractures. Specimen C6-G, galvanized but otherwise identical to specimen

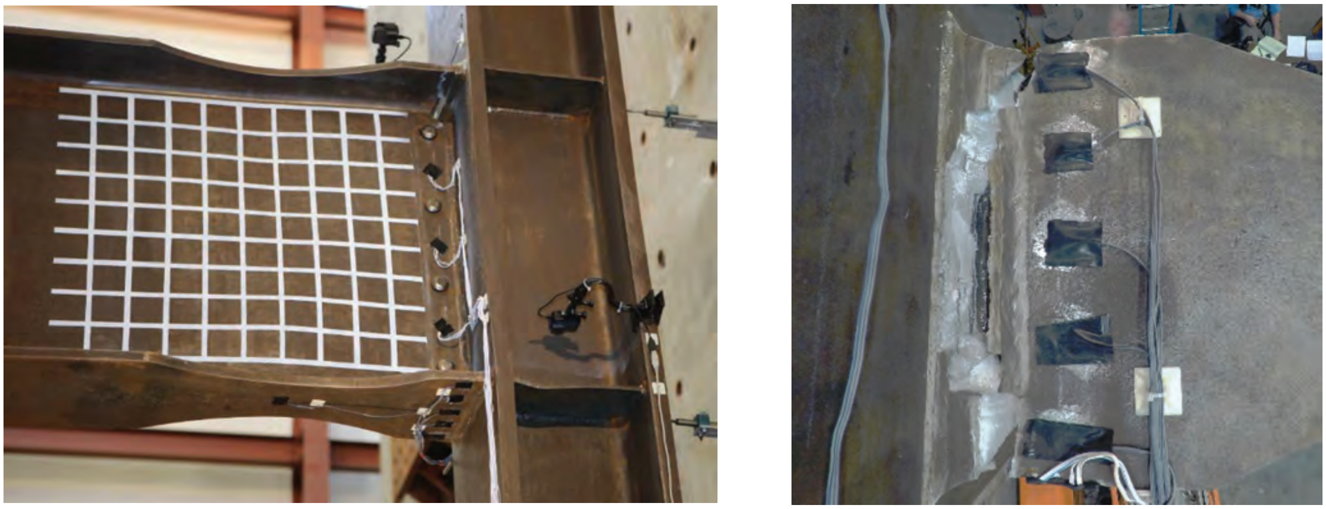
(a) After testing

(b) Top-flange fracture

Fig. 9. Specimen C5 testing results.


(a) After testing

(b) Fracture in top flange CJP groove weld during test

Fig. 10. Specimen C6 testing results.

C6, did not fail at the weld but with a low-cycle fatigue fracture in the reduced beam flange. Based on the experimental and cyclic void growth model results, Reynolds (2020) attributed the likelihood of fracture to the "variability in weld surface topology (i.e., how sharp the reentrant corner is formed between the beam flange and column flange) and variability in weld notch toughness."

Specimen W2's response was initially governed by yielding of the flanges, which started during the 0.0075-rad drift cycles. Beam flange and web local bucking initiated at 0.03 rad. The second cycle at 0.03-rad drift was also the start of a weld fracture in the east beam top flange at the root of the CJP groove weld. The 0.05-rad drift cycles would see a weld tear on the top side of the west beam bottom flange CJP groove weld near the beveled fusion face of the CJP groove weld. A fracture was also observed in the east beam bottom flange CJP groove weld at 0.06-rad drift. These fractures would progress until the second cycle of 0.06-rad drift, when specimen W2 failed by fractures of the east top and west bottom beam flange CJP groove welds, as shown in Figures 11(a) and 11(b). Meanwhile, significant lateral-torsional buckling was observed initially at 0.04-rad drift and, together with flange and web local buckling, was quite severe by the end of the test, as shown in Figure 11(c).

FINITE-ELEMENT STUDIES

A computational parametric study was used to supplement the experimental investigation and verify the proposed methodology (Reynolds, 2020). The finite element analysis (FEA) was validated against the experiments. Parameters included column flange and continuity plate thickness.

The finite element model was validated through comparisons to the experimentally measured load-displacement response of the specimens; observed displacement patterns; and local estimates of accumulated equivalent plastic strain, PEEQ. The beams and columns were modeled as plate assemblies and meshed with shell elements using ABAQUS

(a) Fracture 1 at top flange

(b) Fracture 2 at bottom flange

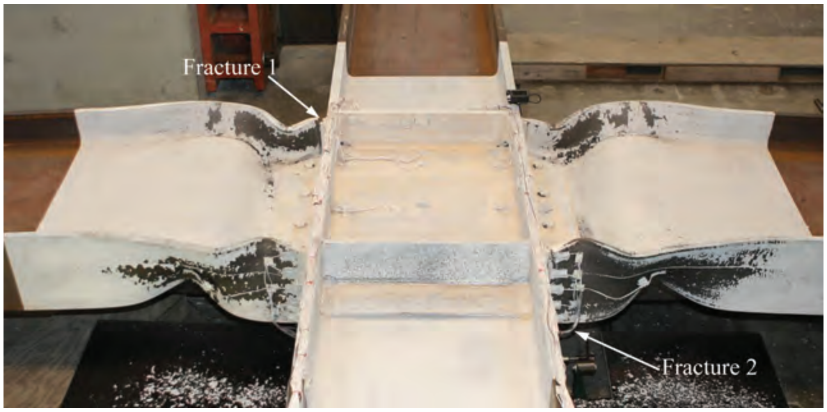

(c) End of test

Fig. 11. Specimen W2 fractures.

CAE (2014). The models did not include the flange-web fillets but did incorporate offsets to properly account for element thickness. The model geometry reflected the appropriate flange cuts in the reduced beam sections and the beam web cuts for the weld access holes. A mixed hardening model in ABAQUS was used for the steel; the mixed model is based on Lemaitre and Chaboche (1990). The cyclic hardening parameters were calibrated using measurements from 23 full-scale, deep-column tests conducted at UCSD (Chansuk et al., 2018). The NLGEOM option in ABAQUS within each explicit analysis step was used to capture geometric nonlinearity. Boundary conditions reflected the test setup and included lateral restraint of the beam at half the beam-depth away from the plastic hinge location. A comparison of the experimental and FEA results for specimen C5 illustrated in Figure 12 shows the ability of the FEA to capture the cyclic, global, load-drift response. The FEA is also able to capture behaviors such as the column kinking and continuity plate local buckling in specimen C5, as shown in Figure 13. Additional details of the model and validation can be found in Reynolds (2020).

Among the parameters investigated during the parametric study were the thickness and width-to-thickness ratio, b/t, of the continuity plate. Effects of normalized continuity plate thickness on continuity plate forces were explored, with comparisons to limit states such as WLY. Given the intentional continuity plate local buckling in specimen C5, the width-to-thickness ratio and instability of the continuity plate were also examined. At high ratios, plate instability resulted in significant bending stresses of the continuity plate. Figure 13 shows local buckling in the FEA of specimen C5 with continuity plate $b/t = 15.7$. Note that $b/t = 16.0$ in the experiment. For plates with a width-to-thickness ratio of 13.5, selected to correspond to $0.56\sqrt{E/R_yF_y}$, local buckling did not occur. The parametric study results suggested that this width-to-thickness limit is applicable to exterior and interior RBS and WUF-W connections.

PROPOSED REVISIONS IN THE AISC SEISMIC PROVISIONS

The experimental program and finite element parametric study have provided a basis for proposed changes to the AISC *Seismic Provisions*. Specifically, a limiting width-to-thickness ratio for continuity plates and the use of fillet welds in lieu of CJP groove welds are recommended. In the test program, the continuity plates with width-to-thickness ratio of 12 did not develop any local instabilities. The computational parametric study confirmed the recommended width-to-thickness limit of $0.56\sqrt{E/R_yF_y}$ for continuity plates. Meanwhile, no failures were observed in the capacity-designed fillet welds connecting the continuity plates to the columns.

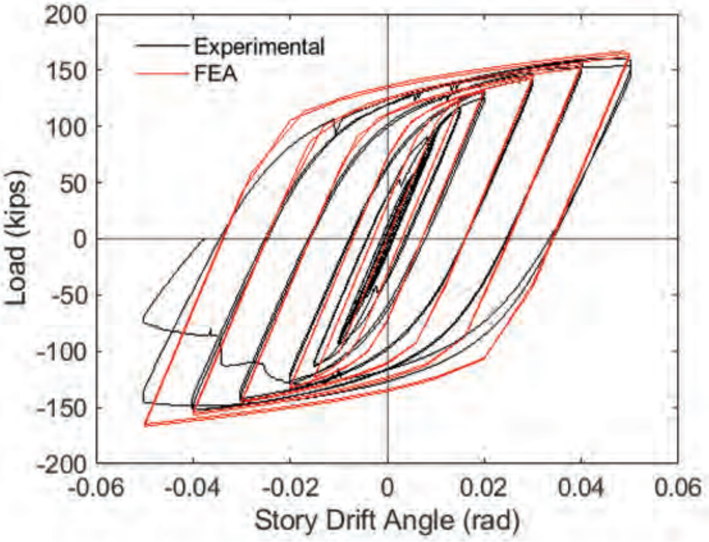

Fig. 12. Comparison of FEA to experimental load-drift response for specimen C5.

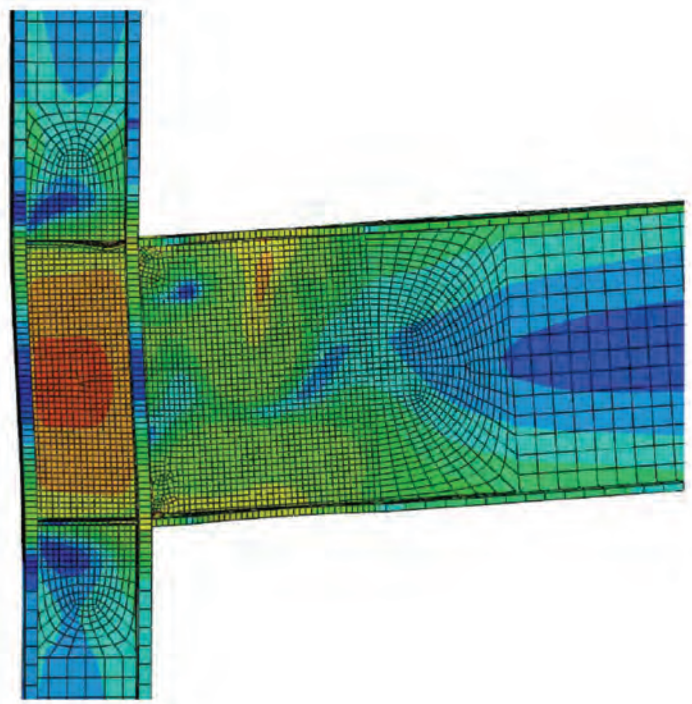

(a) Column kinking in FEA

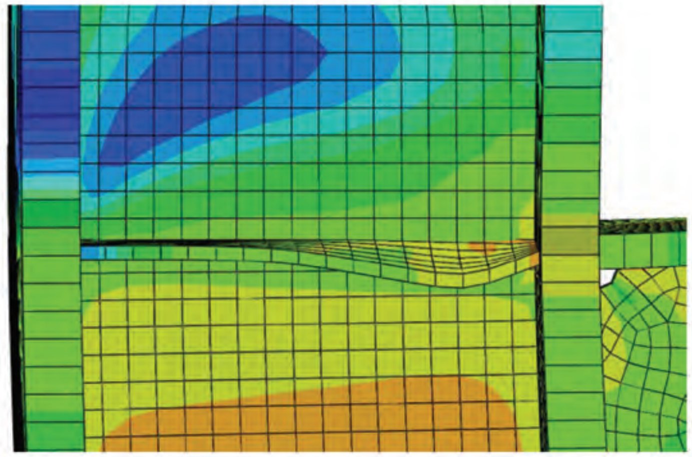

(b) Continuity plate buckling in FEA

(c) Continuity plate buckling in experiment

Fig. 13. Specimen C5 column kinking and continuity plate buckling.

SUMMARY

Recent advances in continuity plate design for special and intermediate moment frames have been highlighted. The comprehensive experimental and computational study by Dr. Mathew Reynolds and Dr. Chia-Ming Uang has supported the development of improved design procedures for continuity plates and their welds. A more efficient plastic design methodology for continuity plates includes procedures for fillet welds instead of CJP groove welds for connecting the continuity plates to the column flanges. Important outcomes of the research include a new continuity plate width-to-thickness limit and a capacity-design rule for sizing the fillet welds. Both provisions have been proposed for the 2022 version of the AISC *Seismic Provisions.*

This article has provided a sampling of the research, a larger effort that also included investigation into provisions for doubler plates. Publications that are in preparation include a detailed experimental results paper and a paper focusing on the parametric FEA results. The experimental results paper will contain design details and results for all test specimens, as well as additional recommendations for continuity and doubler plate design. The finite element analysis paper will provide extensive discussion of the parametric study results that support the proposed design methodology. The experimental results and the associated FEA are also available in Reynolds and Uang (2019) and Reynolds (2020).

ACKNOWLEDGMENTS

Thank you to Dr. Chia-Ming Uang and Dr. Mathew Reynolds for their editorial and other contributions to this article. Special thanks to Dr. Reynolds for all of the materials, coordination, edits, and additional feedback. The research was sponsored by the American Institute of Steel Construction (AISC); Mr. Tom Schlafly and Dr. Devin Huber served as project managers. The Herrick Corporation donated the fabrication of the specimens, and the Smith-Emery Company donated inspection services. The researchers also would like to acknowledge their Advisory Committee: Tim Fraser, Tom Kuznik, Kim Roddis, Subhash Goel, and Brian Volpe, with James Malley serving as the chair. Any findings or recommendations are those of the researchers and do not necessarily reflect the views of the sponsors.

REFERENCES

ABAQUS (2014), *Abaqus Standard User's Manual*, Version 6.14, Dassault Systemes Simulia Corp.

AISC (2016a), *Seismic Provisions for Structural Steel Buildings*, ANSI/AISC 341-16, American Institute of Steel Construction, Chicago, Ill.

AISC (2016b), *Specification for Structural Steel Buildings,* ANSI/AISC 360-16, American Institute of Steel Construction, Chicago, Ill.

AISC (2020), *Prequalified Connections for Special and Intermediate Steel Moment Frames for Seismic Applications*, including Supplements No. 1 and No. 2, ANSI/AISC 358s2-20, Chicago, Ill.

AWS (2016), *Structural Welding Code—Seismic Supplement*, AWS D1.8/D1.8M:2016, American Welding Society, Miami, Fla.

Chansuk, P., Ozkula, G., and Uang, C.-M. (2018), "Seismic Behavior and Design of Deep, Slender Wide-Flange Structural Steel Beam-Columns: Phase 2 Testing," Rep. No. SSRP-18/02, University of California San Diego, San Diego, Calif.

Dowswell, B. (2015), "Plastic Strength of Connection Elements," *Engineering Journal*, AISC, Vol. 52, No. 1, pp. 47–66.

Lemaitre, J. and Chaboche, J.-L. (1990), "Mechanics of Solid Materials," Cambridge International Press.

Mashayekh, A. and Uang, C.-M. (2018), "Experimental Evaluation of a Procedure for SMF Continuity Plate and Weld Design," *Engineering Journal*, AISC, Vol. 55, No. 2, pp. 109–122.

Reynolds, M. (2020), "Alternative Weld Details and Design for Continuity Plates and Doubler Plates for Applications in Special Moment Frames," University of California, San Diego, La Jolla, Calif. ProQuest ID: Reynolds_ucsd_0033D_19175. Merritt ID: ark:/13030/m5xh4zg9. Retrieved from https://escholarship.org/uc/item/32t492xx.

Reynolds, M. and Uang, C.-M. (2019), "Alternative Weld Details and Design for Continuity Plates and Doubler Plates for Applications in Special and Intermediate Moment Frames," Report SSRP-19/03, November, University of California, San Diego, La Jolla, Calif.

Tran, T.T., Hasset, P.M., and Uang, C.-M. (2013), "A Flexibility-Based Formulation for the Design of Continuity Plates in Steel Special Moment Frames," *Engineering Journal*, AISC, Vol. 50, No. 3, pp. 181–200.

ERRATA

Flange Bending in Single Curvature

Bo Dowswell

Vol. 50, No. 2, 2013

Revise Equation 67 to change the negative sign in the second term to a positive sign:

$$K_e = -1.85\left(\frac{e}{c}\right)^3 + 5.23\left(\frac{e}{c}\right)^2 - 5.24\left(\frac{e}{c}\right) + 3.03 \tag{67}$$

Revise the sentence following Equation 67 to:

"From observation of Table 4, the end distance effect can be neglected for all values of b/c if e/c is **greater** than 1.375."

Guide for Authors

Scope *Engineering Journal* is dedicated to the improvement and advancement of steel construction. Its pages are open to all who wish to report on new developments or techniques in steel design, research, the design and/or construction of new projects, steel fabrication methods, or new products of significance to the uses of steel in construction. Only original papers should be submitted.

General Papers intended for publication should be submitted by email Margaret Matthew, editor, at **matthew@aisc.org**.

The articles published in the *Engineering Journal* undergo peer review before publication for (1) originality of contribution; (2) technical value to the steel construction community; (3) proper credit to others working in the same area; (4) prior publication of the material; and (5) justification of the conclusion based on the report.

All papers within the scope outlined above will be reviewed by engineers selected from among AISC, industry, design firms, and universities. The standard review process includes outside review by an average of three reviewers, who are experts in their respective technical area, and volunteers in the program. Papers not accepted will not be returned to the author. Published papers become the property of the American Institute of Steel Construction and are protected by appropriate copyrights. No proofs will be sent to authors. Each author receives three copies of the issue in which his contribution appears.

Manuscripts Manuscripts must be provided in Microsoft Word format. Include a PDF with your submittal so we may verify fonts, equations and figures. View our complete author guidelines at **aisc.org/ej**.

Smarter. Stronger. Steel.

American Institute of Steel Construction
130 E Randolph St, Ste 2000, Chicago, IL 60601
312.670.2400 | aisc.org/ej